FACULDADE DE ENGENHARIA DA UNIVERSIDADE DO PORTO

Experimental investigation of the near-wall flow over transversal moving surface waves

Rui Mário Lemos Ormonde

Integrated Master in Mechanical Engineering

AIA Supervising Academic Member Staff: Dr.-Ing. Wilhelm Jessen

AIA Supervising Professor: Univ.-Prof. Dr.-Ing. Wolfgang Schröder

FEUP Supervising Professor: Prof. Dr. Eng. Fernando Pinho

September, 2014

Experimental investigation of the near-wall flow over transversal moving surface waves

Rui Mário Lemos Ormonde

Integrated Master in Mechanical Engineering

September, 2014

Abstract

The influence of a spanwise transversal surface wave on the near-wall flow field of a turbulent boundary layer is investigated by particle-image velocimetry (PIV) and micro-particle tracking velocimetry (μ-PTV). The experimental setup consists of a flat plate equipped with an insert to generate a transversal spanwise traveling wave on an aluminum surface. PIV and μ-PTV measurements are conducted for three Reynolds numbers, based on the freestream velocity and momentum thickness measured immediately downstream of the actuated surface $Re_\theta = 1200$, 1660, and 2080. The transversal wave is generated by a newly developed electromagnetic actuator system underneath the aluminum surface. Three amplitudes of $A = 0.25$, 0.30 and 0.375 mm at a wave length of $\lambda = 160$ mm and a frequency of $f = 81$ Hz are investigated. The detailed analysis of the velocity profile shows the transversal surface motion to redistribute the velocity in the viscous sublayer and in the logarithmic region of the turbulent boundary layer. The velocity fluctuations in the outer boundary layer are increased and the streamwise momentum in the near-wall regime is lowered. The drag reduction ratio (DR) due to the actuation is determined by the velocity gradient in the viscous sublayer. At the lowest Reynolds number the drag-reducing impact is proportional to the amplitude of the wave. That is, the higher the amplitude, the more pronounced the friction drag reduction, with a DR as high as 3.42% being found in this work, compared to the non-actuated configuration. A vortex-identification method through swirling strength is applied in order to detect changes in the flow structure due to the actuation.

Keywords: drag reduction; PIV measurements, turbulent boundary layer; spanwise traveling wave.

Acknowledgments

I would like to express my special thanks of gratitude:

To Univ.-Prof. Dr.-Ing. Wolfgang Schröder, for welcoming me as MSc thesis student in the AERODYNAMICS INSTITUTE AACHEN and his review of my work.

To my supervisor at AIA, Dr.-Ing. Wilhelm Jessen, who with his kind demeanor was constantly available to assist me in any matter.

To my supervisor at FEUP, Prof. Dr. Fernando Pinho, for his availability and review of my work.

To MSc. Wenfeng Li, PhD student also under Dr. Jensen's supervision at the time of my work in AIA, who acted as main hands-on conductor of the experiments, providing me numerous tips on the experimental setup, explanations on the underlying physical phenomena, help in using the dedicated software, clarifications on results analysis, and who, together with Dr. Jensen, provided general guidance and concern on a daily basis.

To Dipl.-Ing. Pascal Marquardt, for his numerous insights into physical phenomena of drag reduction, detailed explanations of Matlab® programming, besides a thorough review and enhancement of my Matlab® routines to such an extent he must be considered their main author.

To Zhiyin Gin, exchange Bachelor thesis student under MSc W. Li's supervision, who was always ready to help with a high-spirited and persevered mood.

To Dipl.-Ing Dorothee Roggenkamp, for facilitating access to an extensive database of literature.

To Fundação Rotária Portuguesa and its local Rotary Club in Angra do Heroísmo, Terceira Island, Azores, represented in the person of Dr. Aurélio da Fonseca, for their assistance through a scholarship.

To the City Hall of Angra do Heroísmo, who also awarded me with a scholarship under the program BOLSANGRA.

To the Portuguese Ministry of Education and Science, that through its General Directorate of Higher Education grants me a college scholarship.

To the European Commission, for enabling the pursuit of an exchange program under the *ERASMUS - Student Mobility for Placements* mobility scheme.

To Eng. Pedro Brito do Rio, Com.^{or} Fernando Linhares Brum, my godparents Maria Conceição Belerique Ormonde and Jorge Manuel Martins Ormonde.

To my parents, for their constant moral support.

To my sisters, whom I miss.

To João Pedro Ferreira, Tiago Ramos and João Trigueira, my colleagues and friends, for the many fruitful group works and discussions in engineering and non-engineering subjects during these 5 years of learning. They were all of immense help in an academic and personal way.

To Soufiane Haddanni and Tobias Wegner, for their friendship, present all times during my time in Aachen and beyond. To Viera Kopecká, Alvise Barbiero and Eleonora Bonamico, whose

friendship could not also go without mention. To Abel Goes Trzan, whose numerous insights on everything were deemed invaluable.

And finally, to Noreen Küster, for, among many other things, her enduring support, keeping her faith in me, and having blessed me in her company as the fascinating person she is.

Rui Ormonde

"We live on an island surrounded by a sea of ignorance.
As our island of knowledge grows, so does the shore of our ignorance."

John Archibald Wheeler

"Whether you think you can, or think you can't,
you're right."

Henry Ford

Contents

List of Figures

List of Tables

Nomenclature

Roman symbols

A	wave amplitude, mm
c_f	friction coefficient
f	frequency, Hz
Re	Reynolds number
T	temperature, °C
T	time period, s
$\mathbf{u}$	velocity vector, $\mathrm{m\,s^{-1}}$
u, v, w	velocity components in a Cartesian system, $\mathrm{m\,s^{-1}}$
u_τ	friction velocity, $\mathrm{m\,s^{-1}}$
u_∞	freestream velocity, $\mathrm{m\,s^{-1}}$
x, y, z	Cartesian coordinates, mm

Greek symbols

δ	boundary layer thickness, mm
Δ	difference
θ	momentum thickness, mm
λ	Wave length mm
μ	dynamic viscosity, Pa s
ν	kinematic viscosity, $\mathrm{m^2\,s^{-1}}$
ρ	density, $\mathrm{m\,kg^{-3}}$
τ	shear stress, Pa
τ_w	wall friction, Pa

Superscripts

$+$	normalized by the viscous velocity scale u_τ ($\mathrm{m\,s^{-1}}$), the viscous length scale ν/u_τ (m), or the viscous time scale ν/u_τ^2 (s)
$'$	fluctuation of a flow quantity

Overbars

$\bar{}$	temporal mean of a flow quantity

Acronyms

PIV	Particle Image Velocimetry
µ-PTV	Micro-particle tracking velocimetry
DR	Drag reduction
rms	root mean square

Chapter 1

Introduction

"Science has been awaiting the great physicist, who, like GALILEO or NEWTON, should bring order out of chaos in aerodynamics and reduce its many anomalies to the rule of harmonious law", wrote OCTAVE CHANUTE, civil engineer and close friend of the WRIGHT BROTHERS, known for their experiments in flying crafts in aeronautics's early days. CHANUTE died in 1910 without knowing of PRANDTL's work on the boundary layer theory in the early 20th century. PRANDTL's insights in wall-bounded flows, namely the interaction between the body surface and the surrounding fluid by introducing the boundary layer concept, proved to be valuable for subsequent research on fluid dynamics. The so-stated order or rule of harmonious law is far from being reached, but significant progress has been made in detecting coherent structures in the turbulent flow and controlling them in an effort to reduce viscous stresses. PRANDTL himself first used a trip wire to trigger transition from laminar to turbulent flow in the boundary layer, obtaining observable decreases in the shear stress at the wall.

The reader may ask what encourages such viscous stresses reduction. While shape optimization of the moving bodies may considerably reduce the pressure drag, every flow system of technological relevance, such as oil and gas pipelines, high-speed aircraft wings, jet engine intakes and turbine blades, still faces a dramatic energy loss due to the viscous action exerted by turbulence. Indeed, the energy required to propel bodies through a conducting fluid is mainly determined by the dynamical fluid drag, of which about 50% for the case of airplanes is skin-friction drag, which in turn is determined by the wall-shear stress distribution on the wetted area. Figure 1.1 elucidates the drag breakdown in an airplane. Therefore, making our transportation more energy efficient and reducing CO_2 emissions to face rising fuel costs and today's environmental challenges may require changing the way the flow interacts with the surface, i.e. effective flow control mechanisms that promote drag reduction. Further potential advantages are the attenuation of noise, structural vibrations, and aerodynamic heating. The difficulty of implementing that change lies not only in the extreme complexity of the physics underlying turbulence but also in the resistance of such flows to alter favorably when disturbed by external agents. Furthermore, from an economical point of view, one has to ensure that drag reduction strategy brings savings in fuel or energy consumption higher than the costs associated with its functioning.

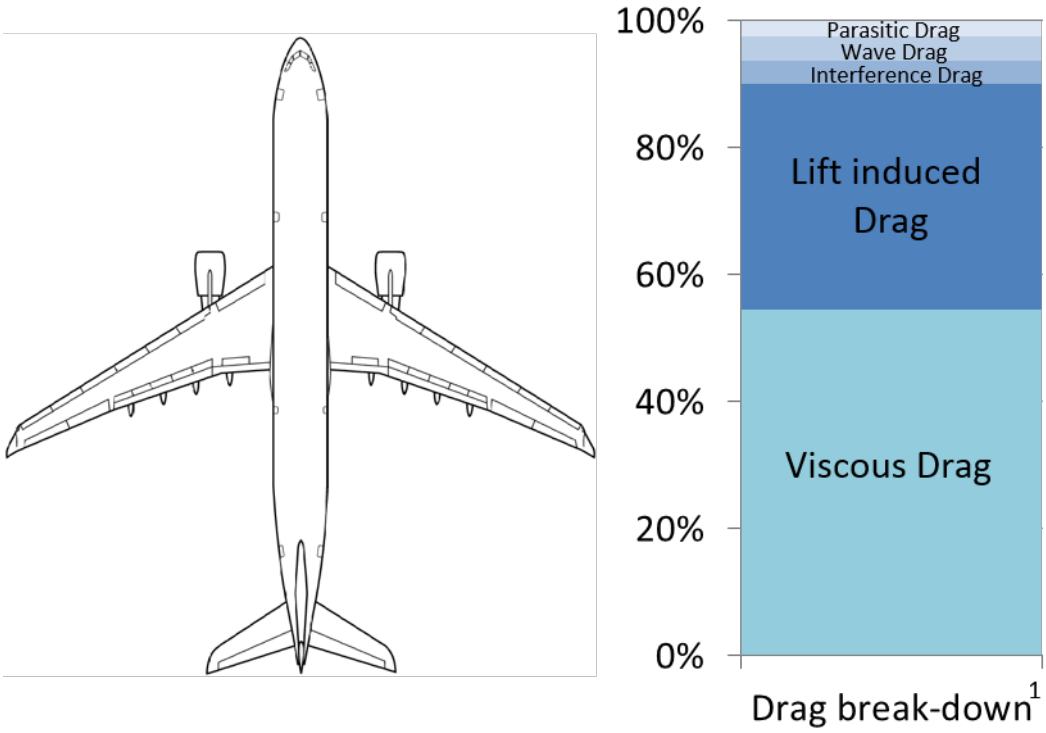

Figure 1.1: Drag break-down in an airplane. The viscous drag is the main contributor, accounting *circa* 55% of the total drag. Therefore, the energy consumption is strongly influenced by the wall-shear stress distribution. [1]

From PRANDTL's early experiments, several other methods have been studied. Most can be divided into passive and active control mechanisms. Passive methods would include employing a geometry on the body's surface known to influence near-wall turbulent structures, like riblets or grooves, while active methods require some sort of external forcing, such as wall oscillations, body forces, cross-flows, etc. In this latter category we include, for instance, direct local feedback control by blowing and suction, feedback control by active dimples, and local wall deformation. Each one changes the near-wall flow field. However, the technical feasibility of the former two is rather difficult: in a high-Reynolds-number regime where length scales are of the order of tens of microns and the timescale is of the order of microseconds, a direct local control approach might be inefficient or not even feasible since it requires a complex high resolution network of sensors and actuators. Another approach is an indirect global control based on influencing the regeneration cycle of near-wall flow field by introducing spanwise and/-or wall-normal velocity components into the near-wall flow field. Although many experiments to this end have been conducted, to this date none has focused on how to implement such alterations to the flow field through a transversal wall motion on a rigid aluminum surface which in general defines the material of standard transport vehicles like airplanes and high-speed trains.

The present endeavor brings forth the documentation and analysis of an experimental work conducted on the latter subject.

1.1 Dissertation Structure

Starting with a literature review in Chapter 2, an overview of the relevant physical quantities to be used is presented as well as of turbulent flow structures of interest. Some turbulence statistics are mentioned and a review of significant publications is performed.

Next, in Chapter 3, the experimental setup is described and the methods followed outlined, by giving an overview of the PIV techniques, prescribing the flow parameters, describing the measurement techniques, mentioning the experimental uncertainties. A vortex counting technique through the swirling strength parameter is also introduced.

In Chapter 4, the results of the velocity profiles, of the root-mean-square value of velocity fluctuations and of the vortex identification and counting are discussed, with concluding remarks and suggestions of future work being done in Chapter 5.

In Appendix A, the Matlab® routines used for the vortex identification and counting are appended. In Appendix B, a preliminary analysis of experimental uncertainty is provided.

Chapter 2

Literature Review

To familiarize the reader with the numerous concepts regarding the field of drag reduction, we structure this literature review in the following manner. First, an overview of relevant physical quantities, to be used throughout this work, is presented accompanied with their meaning and mathematical formulas. Secondly, we describe some of the near-wall structures occurring in turbulent flow, followed by a brief reference to turbulence statistics. The mechanisms for drag reduction are then introduced before presenting some of the techniques that have been used for that purpose and finish the review by referring to the conclusions of some major publications in this field.

2.1 Overview of relevant physical quantities

In an external flow over a flat surface, the outer streamlines of the boundary layer must deflect outward a distance δ^*, the displacement thickness, to satisfy conservation of mass between an upstream and downstream location

$$\delta^* = \int_0^{\delta} \left(1 - \frac{u(y)}{u_\infty}\right) dy \tag{2.1}$$

where y represents the wall-normal coordinate, $u(y)$ is the horizontal velocity component in a two-dimensional flow, and u_∞ stands for the non-perturbed velocity, outside the boundary layer.

To correlate data for a variety of boundary layers under differing conditions, it is usual to use a quantity called momentum thickness, θ, which for incompressible flow can be given by

$$\theta = \int_0^{\infty} \frac{u(y)}{u_\infty} \left(1 - \frac{u(y)}{u_\infty}\right) dy \tag{2.2}$$

There is another quantity, the dimensionless-profile shape factor H, which relates the former two:

$$H = \frac{\delta^*}{\theta}. \tag{2.3}$$

The higher the shape factor, the stronger the adverse pressure gradient. Cebeci and Bradshaw have reported that boundary-layer separation takes place when values of H fall in the range of $1.8 \leq< H \leq< 2.4$, as cited in Castillo's work [2].

Throughout this work, the Reynolds number based on the boundary-layer momentum thickness is used. It is given by

$$Re_\theta = \frac{\rho u_\infty \theta}{\mu} = \frac{u_\infty \theta}{\nu} \tag{2.4}$$

with ρ denoting the fluid density, μ its dynamic viscosity and ν its kinematic viscosity. In all calculations, a value of $\nu = 15.36 \times 10^{-6}\,\mathrm{m^2\,s^{-1}}$ is used , corresponding to air at temperature of approximately 24.5 °C.

For converting quantities to their non-dimensional form, process more briefly referred as *scaling*, it is customary to normalize them by resorting to the viscous velocity scale, given by the friction velocity u_τ, the viscous length scale ν/u_τ, or the viscous time scale ν/u_τ^2. When direct measurement of u_τ is not feasible, it can be determined indirectly by a least-square-linear fitting in the viscous sublayer of a known or measured velocity profile. The friction velocity along with the kinematic viscosity ν is then used to compute the so-called parameters in inner-wall units:

$$\text{Wall-normal coordinate: } y^+ = \frac{u_\tau \cdot y}{\nu} \tag{2.5a}$$

$$\text{Streamwise coordinate: } x^+ = \frac{u_\tau \cdot x}{\nu} \tag{2.5b}$$

$$\text{Spanwise coordinate: } z^+ = \frac{u_\tau \cdot z}{\nu} \tag{2.5c}$$

$$\text{Streamwise velocity : } u^+ = \frac{u}{u_\tau} \tag{2.5d}$$

Replacing u and u^+ by v and v^+ or w and w^+ in Equation (2.5d) yields the wall-normal or spanwise velocity component in inner-wall units, respectively. Regarding the wave parameters, it is also possible to normalize them in inner-wall units:

$$\text{Period: } T^+ = \frac{u_\tau^2}{f \cdot \nu}\text{, where } f \text{ stands for frequency} \tag{2.5e}$$

$$\text{Wave length: } \lambda^+ = \frac{\lambda \cdot u_\tau}{\nu} \tag{2.5f}$$

$$\text{Amplitude: } A^+ = \frac{A \cdot u_\tau}{\nu} \tag{2.5g}$$

2.2 Turbulent flow structures

2.2.1 Streaks

Streaks, which are elongated regions of slow or fast fluid (compared to the mean), more and less aligned in the streamwise direction, are important phenomena occurring in the viscous and buffer layers of near-wall turbulence. They can be visualized by plotting the results of direct numerical simulation (DNS) techniques, as shown in Figures 2.1 and 2.2. Streaks were first identified in 1954 by Hama in his flow visualization experiments. He observed that very close to the wall, the instantaneous spanwise distribution of streamwise velocity consists of alternating regions of high- and low-speed fluids. Since then, streaks have been identified and examined by a number of authors under different experimental conditions. There were investigations in boundary layers subject to different pressure gradients by using the hydrogen bubble wire visualization technique. It was observed that low-speed streaks exist in all cases, including those in which relaminarization can occur [3]. Even after being disrupted, streaks can quickly re-establish. Additionally, streaks show a remarkable degree of persistence and regularity. Experiments in fully turbulent boundary layers conducted during the 1960s and 1970s by different scientists (see review of [4]) provided visualization pictures so similar that it is now acceptable to state that streaks constitute a universal feature of bounded shear flows and that their presence is a sufficient condition for establishing whether a given boundary flow is turbulent.

Many efforts have been made to quantify the physical properties of streaks. Most of the studies focused on the mean spanwise spacing, which for low-Reynolds-number flows ($Re_\theta < 1500$) is found to be around 100 ± 20 wall units. Other studies varying Re_θ up to 10000 reveal an increase of this spacing, indicating its strong dependence on the Reynolds number. [4]

2.2.2 The bursting cycle: sweep and ejection events

Experimental results in the past four decades as well as more recent numerical studies suggest that there is a sequence of self-sustaining activities of near-wall turbulence in boundary layers. Among such turbulence activities, there are two important events, the sweeps and the ejections, in which 80% of the turbulence energy is produced. The ejection-sweep cycle is typically quantified via quadrant analysis, which refers to the joint scatter across four quadrants defined by a Cartesian plane whose abscissa is u' and ordinate is v'. On this layout, we evince four modes of momentum transfer: ejections and sweeps lay on quadrants II and IV while outward and inward interactions are set on quadrants I and III, accordingly. Therefore, the ejections are related to the events accompanying the negative u-component and positive v-component velocity; the sweeps are associated with the positive u-component and negative v-component velocity. When both positive u and v components, the event is called an outward interaction, whereas when both are negative it is named inward interaction. The sweep events are particularly important for drag reduction because they are responsible for the generation of turbulent wall-shear stress. At the same time, they take place close to the wall surface below $y^+ = 15$, suggesting that it is easier to implement

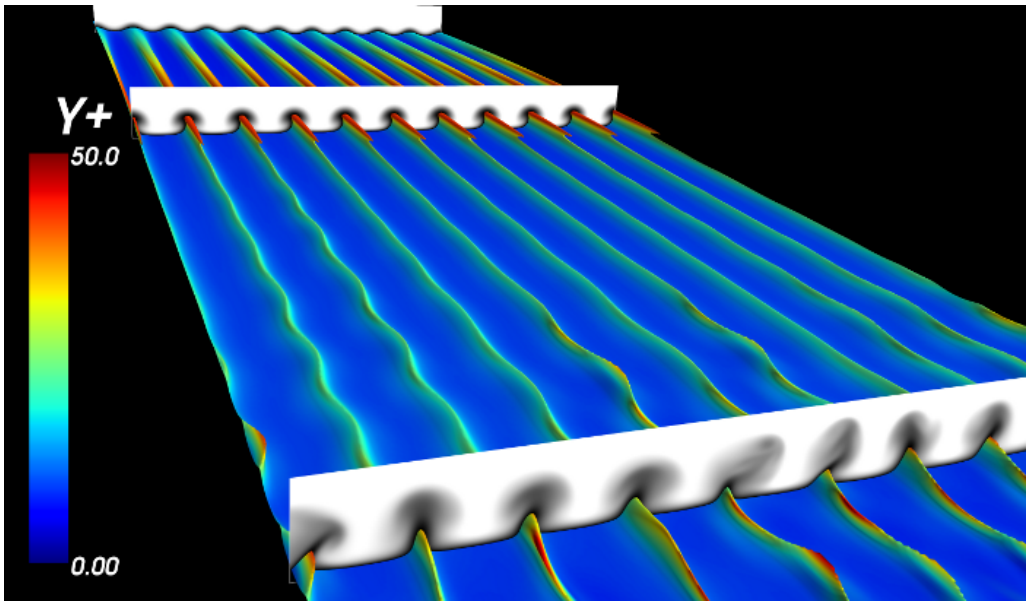

Figure 2.1: 3D view of the streaks growth and breakdown provided by direct numerical simulation of laminar-turbulent transition in channel flow induced by boundary layers interaction. The wall-normal coordinate is defined as $y^+ = (u_\tau \cdot y)/\nu$. Source: http://ufrmeca.univ-lyon1.fr/~buffat/VIDEO/index.html.

wall-based control schemes, such as riblets, spanwise oscillations, and spanwise traveling waves, to obtain turbulent drag reduction. [5]

2.3 Turbulence statistics

It is useful to decompose a velocity field $u(x,y,t)$, henceforth denoted as $\mathbf{u}$, into the sum of an ensemble-averaged component representing a temporal mean, $\overline{\mathbf{u}}$, and a fluctuating component $\mathbf{u}'$, so that

$$\mathbf{u} = \overline{\mathbf{u}} + \mathbf{u}' \tag{2.6}$$

For each physical data point i characterized by its coordinates (x,y), one can compute an *ensemble-averaged component*:

$$\overline{u}_i(x,y) = \frac{1}{N}\sum_{i}^{N} u_i(x,y,t) \tag{2.7a}$$

where N is the number of time steps. An ensemble consists of one or several notionally identical experiments, that is, where the boundary conditions and fluid properties are nominally identical. Each experiment yields a corresponding data-set. Since the ensemble average is computed using the values related to a particular data point, it represents the *temporal mean* of its velocity. Subtracting it from the velocity field, we get a time-dependent *fluctuation component*:

$$u_i'(x,y,t) = u_i(x,y,t) - \overline{u}(x,y). \tag{2.7b}$$

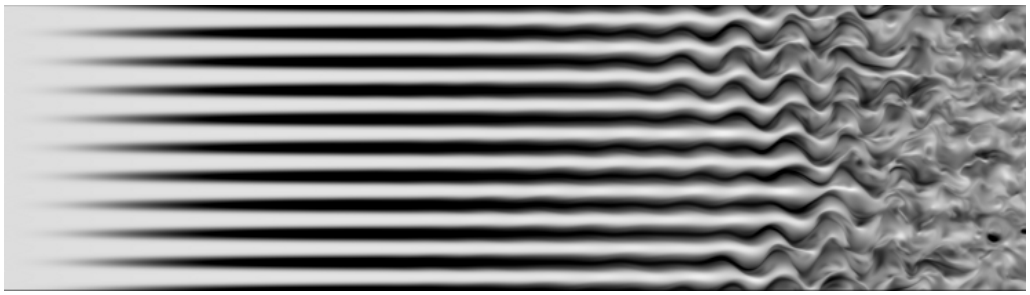

Figure 2.2: Streamwise view parallel to the wall of the streaks referred to in Figure 2.1. Source: http://ufrmeca.univ-lyon1.fr/~buffat/VIDEO/index.html

The spatial vector field $\overline{\mathbf{u}}$ is then time-independent, while the spatial vector field $\mathbf{u}'$ varies in time. When dealing with single data points, we shall hereinafter drop the reference to physical coordinates (x,y), identifying them exclusively with the index i. The root-mean-square (rms) values of velocity fluctuations can be also of use:

$$u_i'^{\text{rms}} = \sqrt{\frac{1}{N}\sum_{i=1}^{N}(u_i')^2} \tag{2.8}$$

especially when determining the rms value of Reynolds stresses:

$$R_i^{\text{rms}} = \rho u_i'^{\text{rms}} \cdot v_i'^{\text{rms}} \tag{2.9}$$

where $v_i'^{\text{rms}}$, denoting the vertical velocity component fluctuation, follows the same computational procedure explained before, replacing $\mathbf{u}$ by $\mathbf{v}$.

2.4 Review of significant publications

In one of the first studies in this area, Jung et al. [6] carried out a direct numerical simulation (DNS) of a planar channel flow (see Figure 2.3) imposing two separate spanwise oscillatory excitation conditions: (i) oscillatory spanwise cross-flow and (ii) spanwise oscillatory motion of a channel wall. It was evinced that for periods of oscillation $T_{\text{osc}}^{+} = \left(T_{\text{osc}} \cdot u_\tau^2\right)/\nu$ in the range of 25 to 200, the turbulent bursting process was suppressed leading to a sustained drag reduction (DR) of 10% to 40% and comparable alterations occurred in all three components of turbulence intensities as well as the turbulent Reynolds shear stress. The optimum oscillation period that allows the most effective suppression of turbulence was found to be $T_{\text{osc}}^{+} = 100$. Also, the results did not depend on whether the type of spanwise oscillatory excitation (cross-flow or wall motion). On the second case, suppression of turbulence only occurred while at the oscillating wall while the flow remained fully turbulent at the other wall.

Touber et al. [8] performed a DNS for a fully developed channel flow, calculating second-moment budgets, joint-probability-density functions, enstrophy quantities and energy-spectra maps.

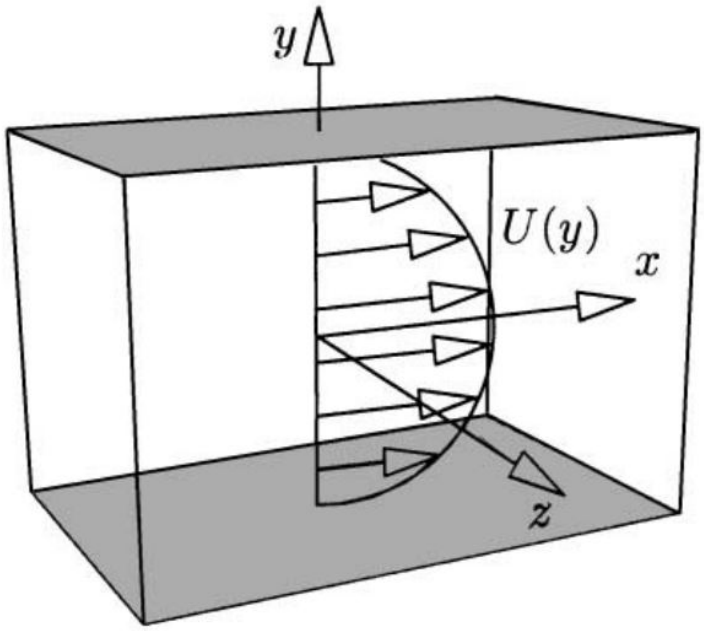

Figure 2.3: Geometry of plane channel flow. The flow is sustained by an externally applied pressure gradient in the x direction. [7]

An unsteady cross-flow straining was shown to cause major spanwise distortions in the streak near-wall structures, which lead to a pronounced reduction in the wall-normal momentum exchange in the viscous sub-layer, sign of a disruption of turbulence contribution to wall-shear stress. The response of the streaks in terms of their periodic reorientation in the wall-parallel planes, as well as their intensity reduction and recovery during cyclic actuation and wall-normal coherence was correlated with temporal variation of the shear-strain vector. A modulating "top-to-bottom" effect, associated with large-scale outer-layer structures was deemed responsible for the reduction in actuation efficiency as Reynolds number increased.

The velocity skewness, defined as the wall-normal derivative of the angle of the velocity vector, was shown to have a significant role in the streak-damping process during the drag reduction phase. This observation was carried out by Agostini and colleagues [9] in a DNS of a channel flow with oscillatory spanwise wall motion with relatively high Reynolds number of the flow ($Re_\tau = 1000$).

Analyzing a previous experimental study, Du et al. [10] performed a simulation of a multi-phase electro-magnetic control. In terms of experimental investigations, they also employed a traveling wave excitation induced by a spanwise Lorentz force and a spanwise oscillation with the same type of force. Turbulence statistics for both cases were reported to be similar; but near-wall structures appeared to be different: in spanwise oscillatory excitation wall-streaks are clearly present whereas in the traveling wave excitation they disappear. A major finding was that the appropriate enhancement of the streamwise vortices could cause a weakening of the streak intensity (as measured by the normal vorticity component, ω_x), and therefore substantial suppression of turbulence production. The optimum oscillating frequency was found according to the following

reasoning: on one hand, the edge of the Stokes layer generated by the oscillating wall is close to 2.5 in non-dimensional units above the wall defined by $y^* = y\sqrt{\omega/(2\nu)}$. On the other hand, the location of the center of near-wall streamwise vortices is about 15 in wall units defined by $y^+ = yu_\tau/\nu$. Combining both equations and solving in order to ω yields a corresponding period $T^+ = 100$. At the frequency corresponding to this period, the Stokes layer generated by the oscillating wall interferes with the turbulence production cycle by suppressing the bursting and sweeping events to the greatest extent, that is, leading to the maximum drag reduction (DR). Superimposing a small streamwise force (up to 10% of the spanwise force) causes no adverse effect on drag reduction. However, when it reaches 50% no DR occurs and from then on the drag force increases compared to the uncontrolled case.

Berger et al. [11] carried out a DNS of turbulent channel flow at low Re_τ (100, 200, 400) to examine the effectiveness of using a Lorentz force to reduce skin friction. They employed embedded electrodes and permanent magnets in the flow surface over which the flow would pass. In a first approach based on a open-loop control scheme, a temporally oscillating Lorentz force caused skin-friction to be reduced by 40%, but the power needed to generate the Lorentz force was 10 times larger than the power saved due to reduced drag. Efficiency would further decrease with increasing Re_τ. In a second approach they employed a closed-loop control scheme: a idealized wall-normal Lorentz force was being effected upon detection of near-wall turbulent events responsible for high-skin friction. In this manner, drag was significantly reduced with greater efficiency. As a conclusion, it was stated that the use of this Lorentz force could result in a net decrease of power required to propel objects through viscous conducting fluids.

Breuer [12] designed, fabricated and tested a Lorentz force actuator achieving similar trends to those of Du [10, 13] and Berger [11].

Quadrio and co-workers [14] performed a DNS of a plane turbulent channel flow with sinusoidal waves of spanwise velocity which vary in time and are modulated in space along the streamwise direction. When slow waves were used in forward direction, there was drag reduction, but an increase in their speed maintaining the same direction caused *drag increase* (DI). However, further increase past that point lead to a change back to drag reduction. On the other hand, with backward-traveling waves, there was drag reduction at any speed. They concluded that drag increase occurs when waves travel at a speed comparable with that of the convecting near-wall turbulence structures. In their analysis they studied the effects of parameters such as wave number k_x, temporal frequency ω, forcing amplitude A and Reynolds number Re. On top of that, a global energy budget was also addressed, evidencing that minimum generation power was needed when DR is maximum, which confirmed the existence of net savings. Besides, it was observed that with DI, structures are tilted whereas with DR they remain aligned with the streamwise direction.

Ricco et al. [15] conducted a DNS of a turbulent channel flow with harmonic oscillation of the walls, carried out at constant pressure gradient. The DR manifested itself as increased mass flow rate. Energy and enstrophy balances were taken into account, showing that both viscous dissipation of the mean flow and of turbulent fluctuation increase with the mass flow rate, but the relative importance of the second decreases. In terms of turbulent enstrophy, at the early stages of

wall motion, the dominant, oscillation-related term in the turbulent enstrophy is shown to cause the turbulent dissipation to increase, before slowly reaching the new quasi-equilibrium state. This is the mechanism for the increase in mass flow rate, which is a manifestation of drag decrease. It was also shown that the time-average volume of this term related linearly to DR.

Zhou et al. [16] performed a DNS of low Reynolds flow ($Re = 180$) where two flow configurations were compared: (a) constant streamwise pressure gradient and (b) constant streamwise flow rate, both with spanwise oscillating wall. For the first case, DR increases with peak wall speed while for the second, DR increases with increasing wall speed and then levels out, agreeing with experimental data. At $W_p^+ \leq 20$ both exhibit comparable DR, with a maximum of 42%. The energy input that is required makes for the small net gain of around 5%, undermining the economical practicability for the cases studied. In terms of turbulence statistics in oscillating channel, a outward shift in the profiles was observed, while some turbulent quantities are increased, but others are decreased, which contrasts with the oscillating channel at fixed flow rate, where all quantities (u, p and w') are reduced significantly throughout the channel. Also, near-wall structures are altered differently by wall oscillations for the constant pressure gradient flow and the constant mass flow. Nonetheless, numerical evidence continues to support that it is the near-wall fluid and streaky structures that have been altered and in turn are responsible for the drag reduction by wall motion.

Ricco et al. [15] made an experimental investigation in a water channel by means of the hydrogen-bubble technique. It was observed that when oscillation starts, low-speed streaks shift laterally, and cyclically incline to an angle with respect to the streamwise direction. Then, the interaction between these low-velocity pockets and overriding longitudinal vortices are strongly altered, the latter being only slightly disturbed by the spanwise Stokes layer which develops due to the wall movement. Ejections of low speed fluid from the viscous sublayer to lighter regions of the boundary layer and sweeping motion of high-speed fluid towards the wall are significantly weakened, the latter due to the shield effect caused by the Stokes layer against them. This sweeping activity is known to be responsible for high wall-shear stress. Furthermore, it was shown that turbulent structures are already remarkably affected just after one oscillating cycle. In addition, a cyclic tilting of streaks with respect to the streamwise direction was observed, their length was reduced and the spacing between them increased. Downstream of the wall section, the flow recovers its natural state by transmitting the transversal oscillatory motion of the low-speed streaks upward to the longitudinal vortical structures by means of viscous diffusion. Structures at higher regions from the wall now oscillate laterally, while the streaks orient in the streamwise direction, similarly to the natural turbulent flow.

Akhavan et al. [17] conducted a DNS of planar turbulent channel flow comparing two cases: oscillatory spanwise crossflow and oscillatory spanwise motion of one wall. They verified that production of turbulence is suppressed for $25 < T_{osc}^+ < 200$. Also, with $T_{osc,opt}^+ = 100$, 62% reduction is achieved in turbulent production and 40% in drag reduction. Also, they noted a continual shift of the near wall streamwise vortices relative to the wall layer streaks leading to a widening, merging and weakening of the wall layer streaks, understood as responsible for the suppression of

turbulence.

Baron and co-workers [18] resolved the Navier-stokes equations in a numerical simulation in a plane channel flow. Fixing the frequency, the amplitude of oscillation was determined taking into account the amount of friction reduction, overall energy balance and power spent for wall motion. It was shown that spanwise oscillation of the wall is an effective method for sustained friction drag reduction for low Reynolds ($Re_\tau = 100$) in wall-bounded turbulent flows. However, savings in friction were counterbalanced by the power needed to sustain the wall motion. A positive balance - which did not include mechanical systems losses - only occurred when the amplitude of velocity oscillation was low. As for turbulence statistics, a reduction of velocity fluctuations was observed, mainly in the normal component, v, was observed, as well as an outward shift of most profiles, denouncing a growth in thickness of the traverse boundary layer induced by the moving wall. Also, the transversal boundary layer produced by the oscillation was characterized by reduced turbulent activity. The authors stated that in spite of difficult technical feasibility, the accurate comprehension of local spanwise motions would highlight their role in the overall cycle of production and regeneration of turbulence.

In experiments done on a open-return, low speed wind tunnel, Choi and work colleagues [19] investigated the effects of a spanwise wall oscillation. They noted a reduction of the mean velocity gradient of the turbulent boundary layer close to the wall and a upwards shift in the logarithmic velocity profile by the wall oscillation. It was argued that the changes in the velocity profile were due to negative spanwise vorticity created in the near-wall region of the boundary layer over the oscillating wall. As near-wall velocity dropped, there was a reduction in the stretching of the quasi-streamwise longitudinal vortices, causing the friction drag to diminish. This was also evinced in the sweep events, whose duration fell by 78% and strength by 64%. In a corresponding 2D numerical model, they fell by 47% and 23%, respectively. By phase-averaging conditionally sampled velocity data, it was shown that the frequency of the sweep events had been reduced with the reduction in the streamwise velocity when the negative spanwise vorticity was created by the wall oscillation and also that a DR of 45% could be achieved for $w^+ = 15$.

Chapter 3

Experimental Setup and Methods

In this chapter, an overview of the PIV technique is provided focusing on its basic principles and general equipment. Later on, the details of both particular PIV and μ-PTV techniques employed in this work are given, including the specification of flow parameters, specific material setup and correlation software used. Furthermore, a brief reference to the experimental uncertainties is made. The chapter ends introducing a method for identifying and counting vortical structures based on a scalar-field parameter called swirling strength.

3.1 Overview of the PIV technique

Particle Image Velocimetry (PIV) is a nonintrusive, indirect, whole-field technique to measure fluid motion, providing instantaneous velocity vector measurements in a cross-section of a flow. Two velocity components are measured (2C-PIV), but use of a stereoscopic approach permits all three velocity components to be recorded, resulting in instantaneous 3D velocity vectors for the measurement plane. In this work, only 2C-PIV is used. It is a digital processing technique in two steps: acquisition and analysis, whereupon the use of CCD (charged-couple device) or CMOS (complementary metal–oxide–semiconductor) cameras and dedicated software results in real-time velocity maps. The results that PIV provides are similar to computational fluid dynamics, i.e. large eddy simulations, and real-time velocity maps are an invaluable tool for fluid dynamics.

In PIV the velocity vectors are derived from sub-sections of the target area by measuring the movement of particles between two light pulses - which define a time step: the basic principle is then to take two snapshots of the flow field at this known time interval, and evaluating the velocity with $U = \Delta s/\Delta t$, as depicted in Figure 3.1.

The main features of the PIV technique may be summarized in the following list:

- The technique is non-intrusive and measures the velocities of micron-sized particles following the flow.
- The allowed velocities range from zero to supersonic.
- Provides instantaneous velocity vector maps in a cross-section of the flow.

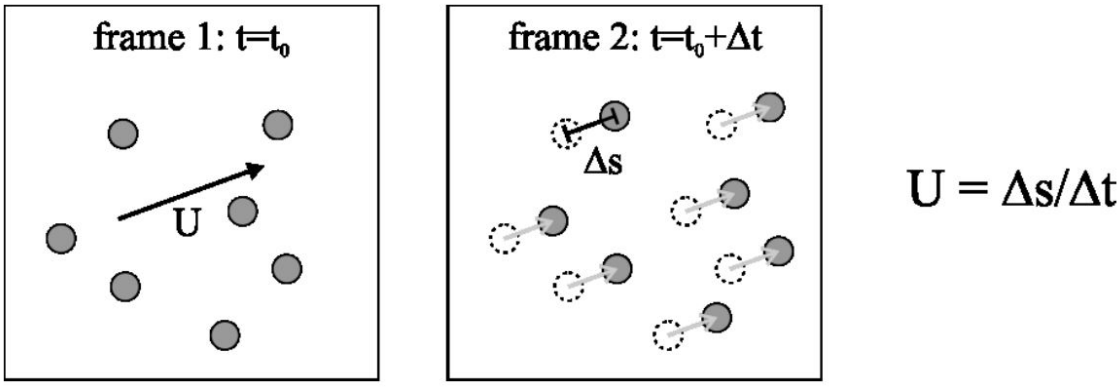

Figure 3.1: PIV basic principle: retrieving particles' velocity by measuring the distance traveled within a known time interval.

- All three components in a plane may be obtained with the use of a stereoscopic arrangement.
- With sequences of velocity vector maps, statistics, spatial correlations and other relevant data are available.
- With fast CMOS technology and powerful lasers, measurements in the kHz can be made.

In Figure 3.4 an illustration of this technique is provided, where several concepts and equipment are placed in the method's logical sequence: the light source (double-pulsed laser), the shaping optics (cylindrical lens), the light sheet, the measurement volume inside the target area, the imaging optics (camera), the correlations between paired image frames, the retrieved raw data (point coordinates and velocities in two components) and the analysis data in terms of derived and statistical quantities (vorticity, averages, RMS values, etc.). For instance, a vorticity contour plot can be derived from the velocity map, Figure 3.1. In Figure 3.5, the specific arrangement of the PIV technique to a wind tunnel is provided in a three-dimensional schematics.

Once a sequence of two light pulses is recorded, the images are divided into small subsections called interrogation areas (IA). The interrogation areas from each image frame, I_1 and I_2, are cross-correlated with each other, pixel by pixel. A visual description of the correlation process is provided in Figure 3.3. The correlation produces a signal peak, identifying the average particle displacement, ΔX. An accurate measure of the displacement - and thus also the velocity - is achieved with sub-pixel interpolation. A velocity vector map over the whole target area is obtained by repeating the cross-correlation for each interrogation area over the two images frames captured by the camera. This correlation process is visually schematized in Figure 3.3.

In terms of equipment, the main components are:

Powerful light source - laser: which needs to be bright, monochromatic (single wavelength), able to be bundled, redirected and formed into a sheet. The laser can be either of continuous-wave type or of pulsed type. In a twin laser, two cavities generate each an independent pulse.

Optics: required to turn the point-shaped laser light into an evenly illuminated flat 'sheet' inside the field of interest. To form a laser-beam into a sheet, a system of concave, cylindrical

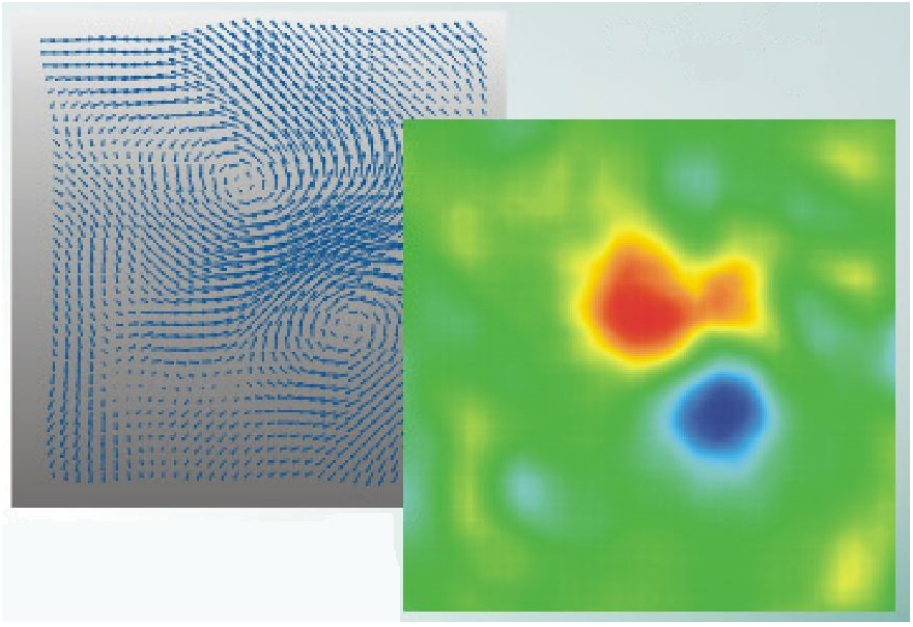

Figure 3.2: Velocity vector map and derived vorticity, $\omega = \partial v/\partial x$ - $\partial u/\partial y$, contour plot. The range of colors in the plot goes from red to blue, denoting positive to negative values of vorticity, with green representing zero-vorticity areas.

and convex lenses is used like in Fig 3.6. The beam is first widened uni-directionally by a concave lens until it arrives at a cylindrical lens, such as that of Figure 3.7. There it is first focused due to a convex profile on the side view's plane. The other plan is unaffected by the convexity shape. After passing the the third lens, which is biconvex, the progressively focused light sheet reaches the focal point and starts to spread beyond that. On the other plane, it will gradually reduce its width. The desired sheet thickness can therefore be varied by changing the focus of the third lens.

Seeding: What is directly measured by PIV is the particle motion, not the fluid motion. In order for the former to be representative of the latter, the following requirements must be satisfied: (a) particle size small enough to follow the flow neutrally. Big particle sizes would cause disruptions in the flow structures and velocity field; (b) same density as the fluid, neither buoyant nor sinking; (c) particles big and reflective enough to provide a good scattered light image; (d) cheaply available or easy to generate; (e) homogeneous in size and behavior; (f) non-toxic, chemically inactive. In air flows, some common particles are smoke ($< 1\,\mu m$), Di-Ethyl-Hexyl-Sebacat, acronymized as DEHS ($0.5 - 1.5\,\mu m$) and Helium-filled soap bubbles ($1 - 3\,mm$). DEHS has the advantage of evaporating after a few hours, taking 4 h for a 0.3-µm droplet; (g) correct amount of particles: the number of particles in the flow is of some importance in obtaining a good signal peak in the cross-correlation. As a rule of thumb, 10 to 25 particle images should be seen in each interrogation area.

Camera(s): which need to have a fast image rate, good resolution (typically 1000×1000 pixels, up to $4000 \times 4000 = 16$Mpixels. Two sensors techniques are commonly available: (1)

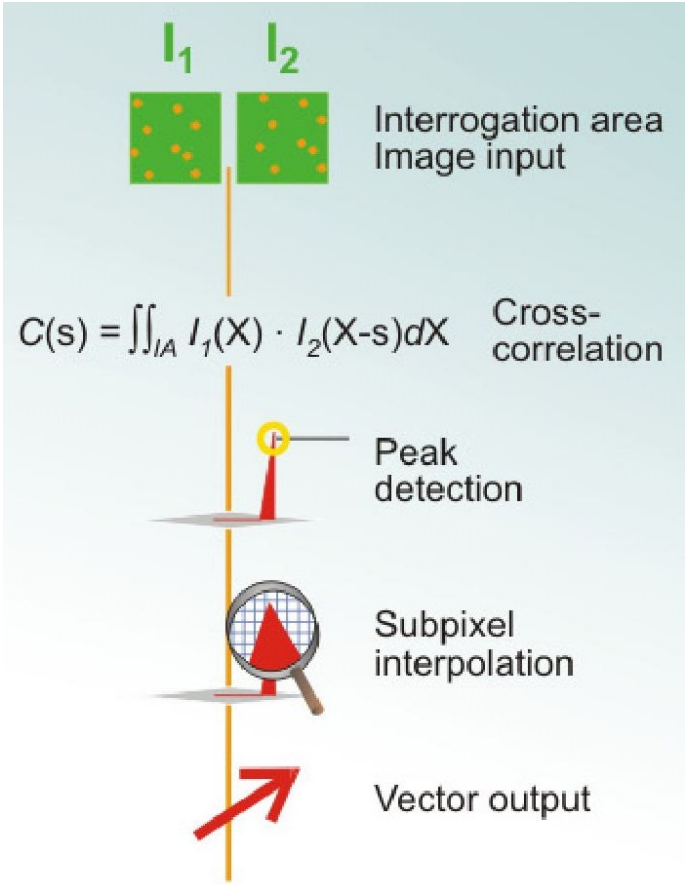

Figure 3.3: The correlation of the two interrogation areas, I_1 and I_2, results in the particle displacement ΔX, represented by a signal peak in the correlation $C(\Delta X)$. [20]

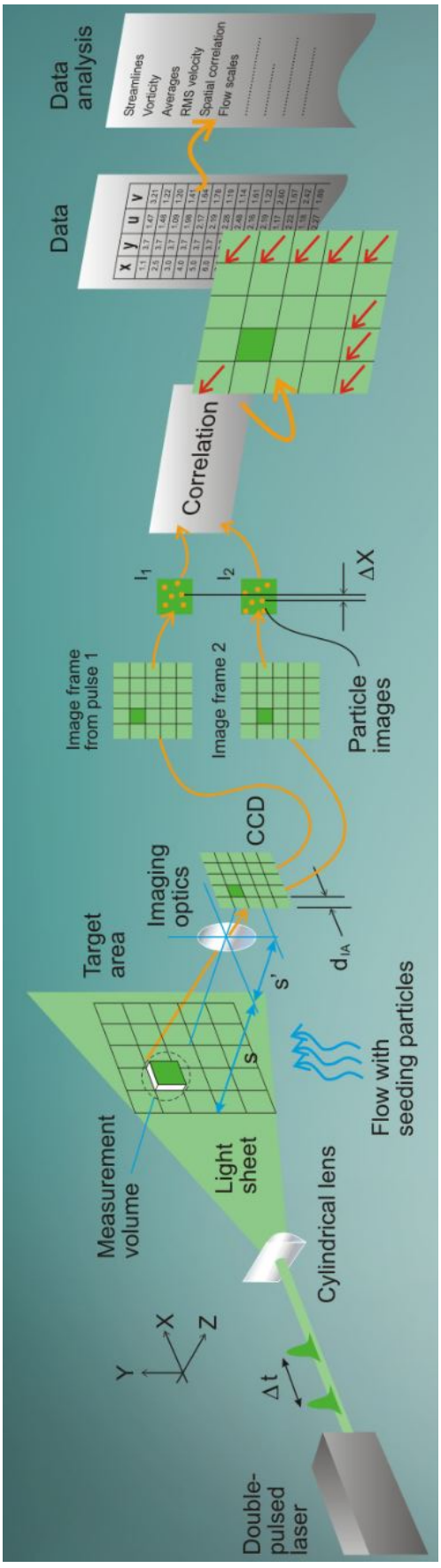

Figure 3.4: Conceptual illustration of the PIV technique, from light source to data analysis. [20]

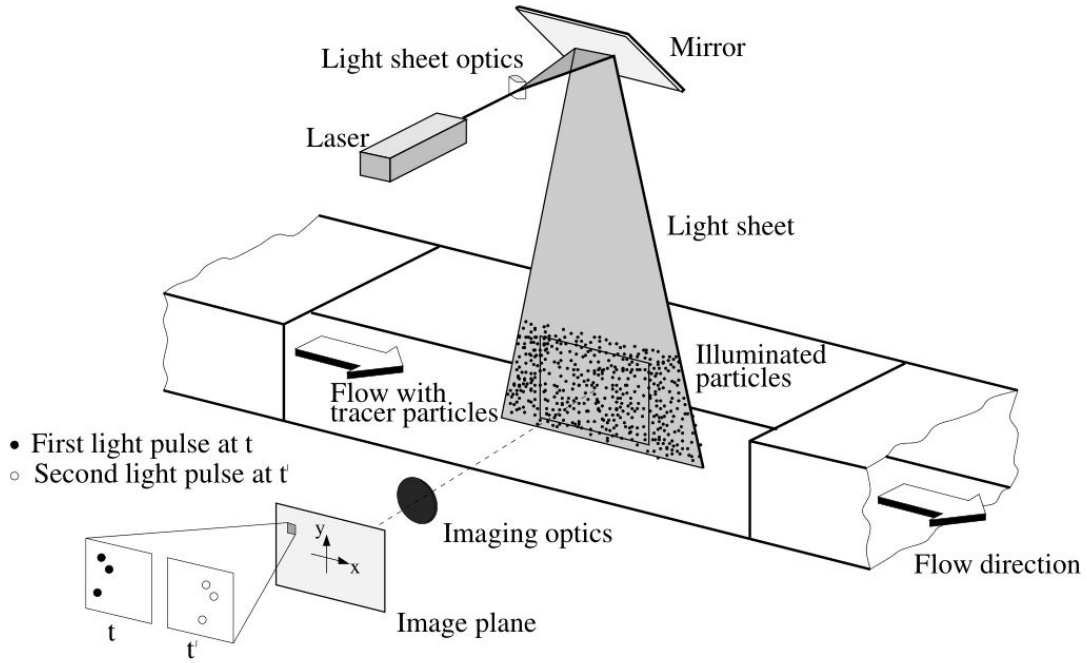

Figure 3.5: Experimental arrangement for particle image velocimetry in a wind tunnel. [21]

Charged-couple device (CCD) – this one is fast in recording double-frames (2 pictures, more than 1 ms apart) albeit slower in overall acquisition rate ($1-20$ Hz), provides the best signal-to-noise ratio and highest sensitivity, besides being an established technology. (2) Complementary metal–oxide–semiconductor (CMOS) – it is a fast developing technique that guarantees the highest frame rates (500, 1000 even 5000 Hz), allowing image subsections to be picked even for higher speeds.

Synchronization: Normally synchronization is achieved by means of a sync generator or synchronizer acting as a timing unit to control the camera shutter and the laser. The connections of the sync generator to the remaining PIV/µ-PTV setup can be seen in Figure 3.8. In PIV, it is required that two particle images are taken with a very short time separation, typically less than 100 µs. A technique called frame straddling enables recording of two images with a time separation as little as 100 ns. In this technique, the diode-pumped Nd:YLF or Nd:YAG laser is pulsed twice, thereby *straddling* the two frames as shown in Figures 3.9 and 3.10. The quantity specified as "Dt" is the pulse distance. Once the synchronizer emits the signal to the Sync In terminal of the camera, its shutter is open. Then, using the camera's built-in delay function, a transistor–transistor logic (TTL) pulse is sent through its Sync Out terminal to trigger the laser at every second frame. The pulse distance is big enough to accommodate the time between closing and re-opening of the camera's shutter. To control the synchronizer, either an external triggering event, such as a propeller revolution, or a fixed acquisition rate can be specified, as depicted in Figure 3.11. Figure 3.12 clarifies what is understood as acquisition rate.

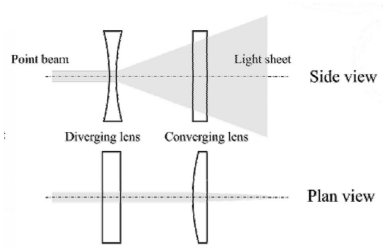

Figure 3.6: Production of a laser sheet.

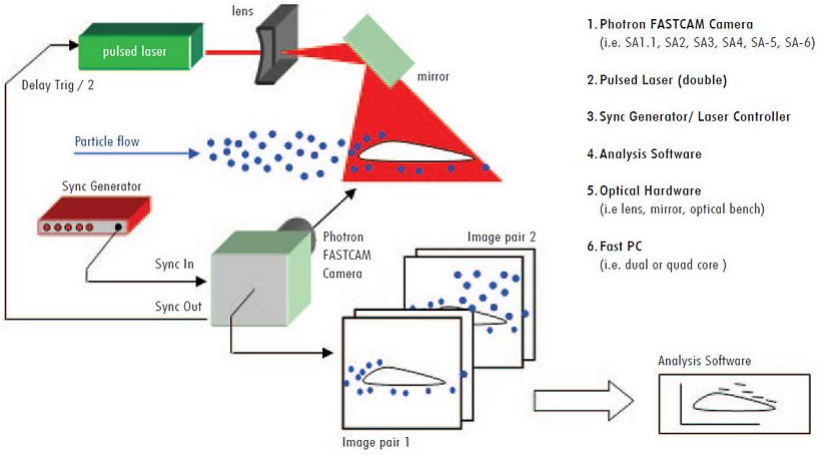

Figure 3.8: Sync generator task in the PIV/µ-PTV setup, acting as laser and camera shutter controller. Source: http://www.photron.com/?cmd=casestudy&type=piv.

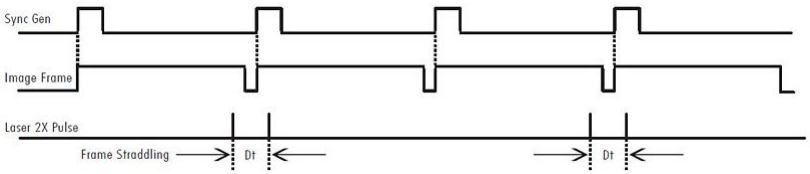

Figure 3.9: Relationship between synchronizer, image frame and laser pulse signal. Source: http://www.photron.com/?cmd=casestudy&type=piv.

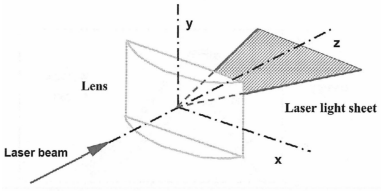

Figure 3.7: Sketch of a cylindrical lens

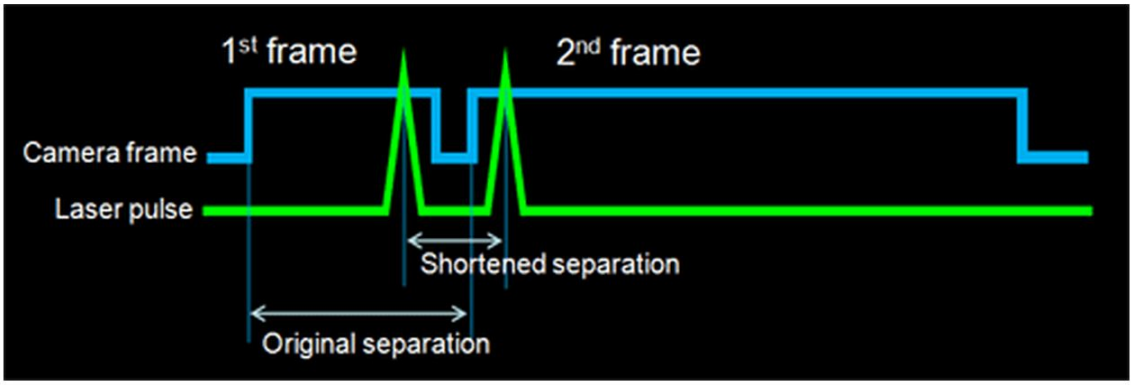

Figure 3.10: Frame straddling signal diagram. Source: hhttp://www.seika-mt.com/product/piv-en/Principle_of_PIV.html.

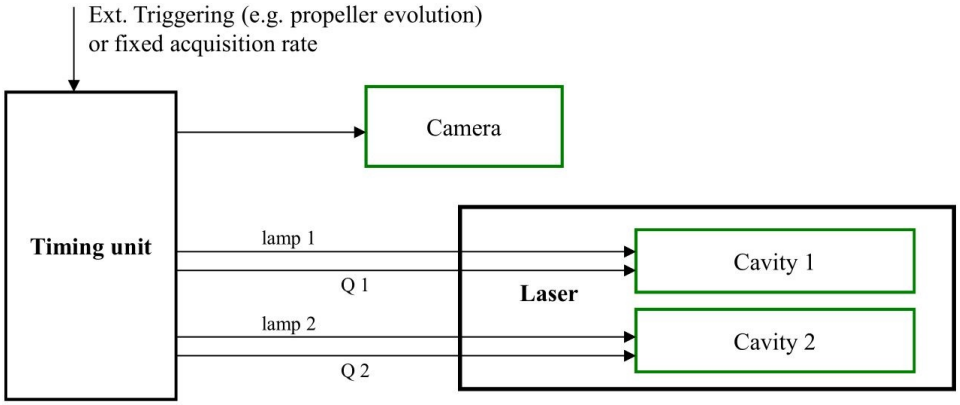

Figure 3.11: Controlling of the synchronizer (timing unit) via fixed acquisition rate or external triggering event, such as a propeller revolution.

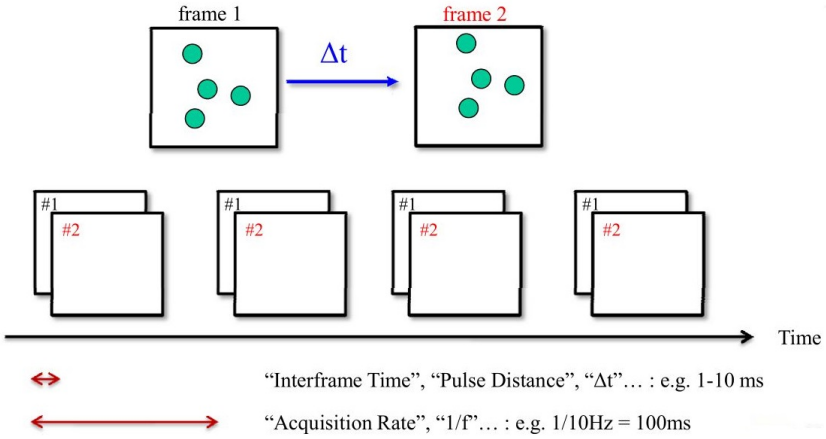

Figure 3.12: Fixed acquisition rate concept.

Software: that can carry out the image acquisition (adjusting measurement parameters, controlling hardware devices, creating image database with acquired information), and the data analysis (image processing/enhancement - when needed, masking of unwanted areas, analysis of each image pair through correlation methods that yield a vector map, visualization, computation of statistical quantities, exporting results), or a software package that can do both.

The following consideration regards the spatial resolution. Setting up a PIV measurement, the side length of the interrogation area, d_{IA}, and the image magnification, s'/s – see Figure 3.4, are balanced against the size of the flow structures to be resolved. One way of expressing this is to require velocity gradients to be small within the interrogation area:

$$\frac{\frac{s'}{s} \cdot |v_{\max} - v_{\min}|_{\mathrm{IA}} \cdot \Delta t}{d_{\mathrm{IA}}} < 5\% \tag{3.1}$$

In terms of dynamic range, the highest measurable velocity is constrained by particles traveling further than the size of the interrogation are within the time Δt. The result is lost correlation between the two image frames and thus loss of velocity information. As a general rule, the following requirement should be observed:

$$\frac{\frac{s'}{s} \cdot v \cdot \Delta t}{d_{\mathrm{IA}}} < 25\% \tag{3.2}$$

When the size of the interrogation area, the magnification of the imaging and the light-sheet thickness are know, the measurement volume can be determined.

3.2 Experimental setup and flow parameters

The experimental setup consists of a flat plate with a well finished surface mounted in the open $1.8\,\mathrm{m} \times 1.2\,\mathrm{m} \times 1.2\,\mathrm{m}$ test segment of a low speed closed-loop wind tunnel (Göttingen-type). The

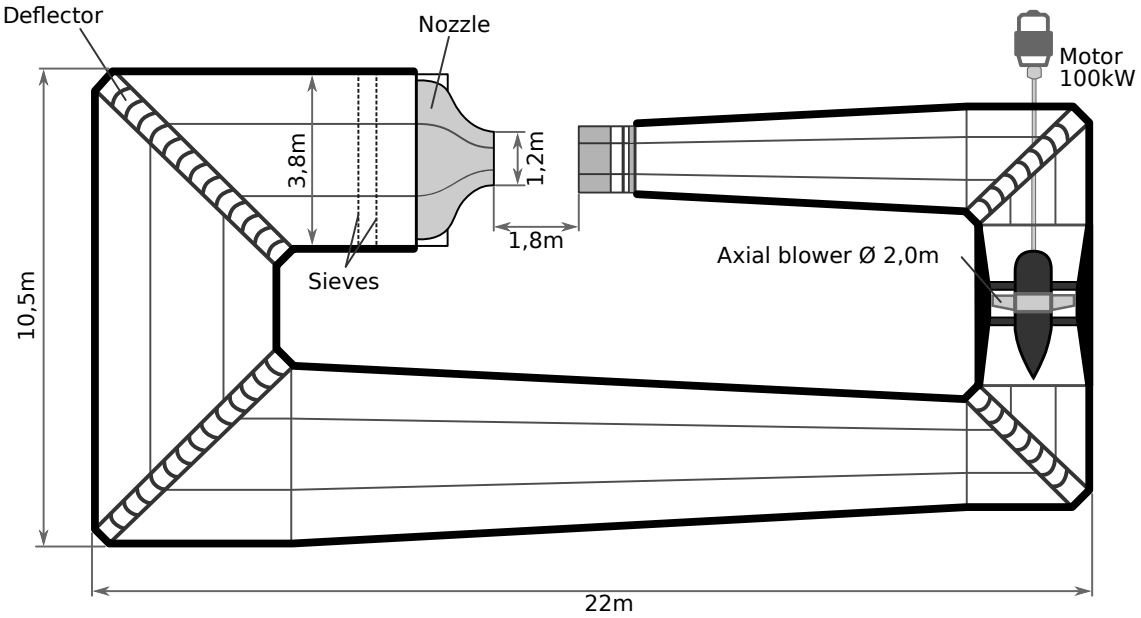

Figure 3.13: Schematics of the Göttingen-type wind tunnel in the Aerodynamics Institute Aachen.

flow over the flat plate undergoes a zero streamwise pressure gradient. A schematics of this tunnel, present in Aerodynamics Institute Aachen, is provided in Figure 3.13. The center of the flat plate is equipped with an insert that actuates a 0.3 mm-thick aluminum sheet of $400 \times 400\,\mathrm{mm}^2$ with a traveling sinusoidal wave. Figure 3.14 shows a sketch of the flat plate mounted in the open test segment of the wind tunnel indicating the actuated surface with its center located 0.66 m downstream of the leading edge. The boundary layer is tripped at the leading edge to generate a fully developed turbulent boundary layer. The sketch in Figure 3.14 also shows the position of the laser light sheet along the centerline of the PIV/μ-PTV setup and the corresponding camera arrangement.

The electromagnetic actuator system underneath the aluminum sheet (Figure 3.15) has been developed by the Central Institute for Electronics (ZEL) of the Forschungszentrum Jülich (Jülich Research Center). This actuator system consists of 10 actuated bars at a lateral distance of 20 mm which are glued parallel to the freestream direction to the lower side of the aluminum sheet. Each bar features a coil in its lower part that consists of 200 windings of 0.125 mm-diameter copper wire as shown in Figure 3.16. Together with the beam and needed mounting pieces, each bar weighs close to 55 g. With a current of 0.5 A, the bars exert a force of about 60 N. The actuator system is operated by a control unit, displayed on Figure 3.17 that allows the generation of wave amplitudes to the aluminum surface up to $A = 0.5\,\mathrm{mm}$ with frequencies in the range of $0\,\mathrm{Hz} < f < 160\,\mathrm{Hz}$. Due to the construction, the minimum wave length of the transversal motion is limited to 60 mm.

Before the measurements, the amplitude of each bar is checked by a laser displacement sensor with a repeatability of 20 mm, a sampling rate of 20 kHz, and a measurable range of $\pm 3\,\mathrm{mm}$. During the measurements the amplitude and phase are monitored by acceleration sensors fixed to the bars.

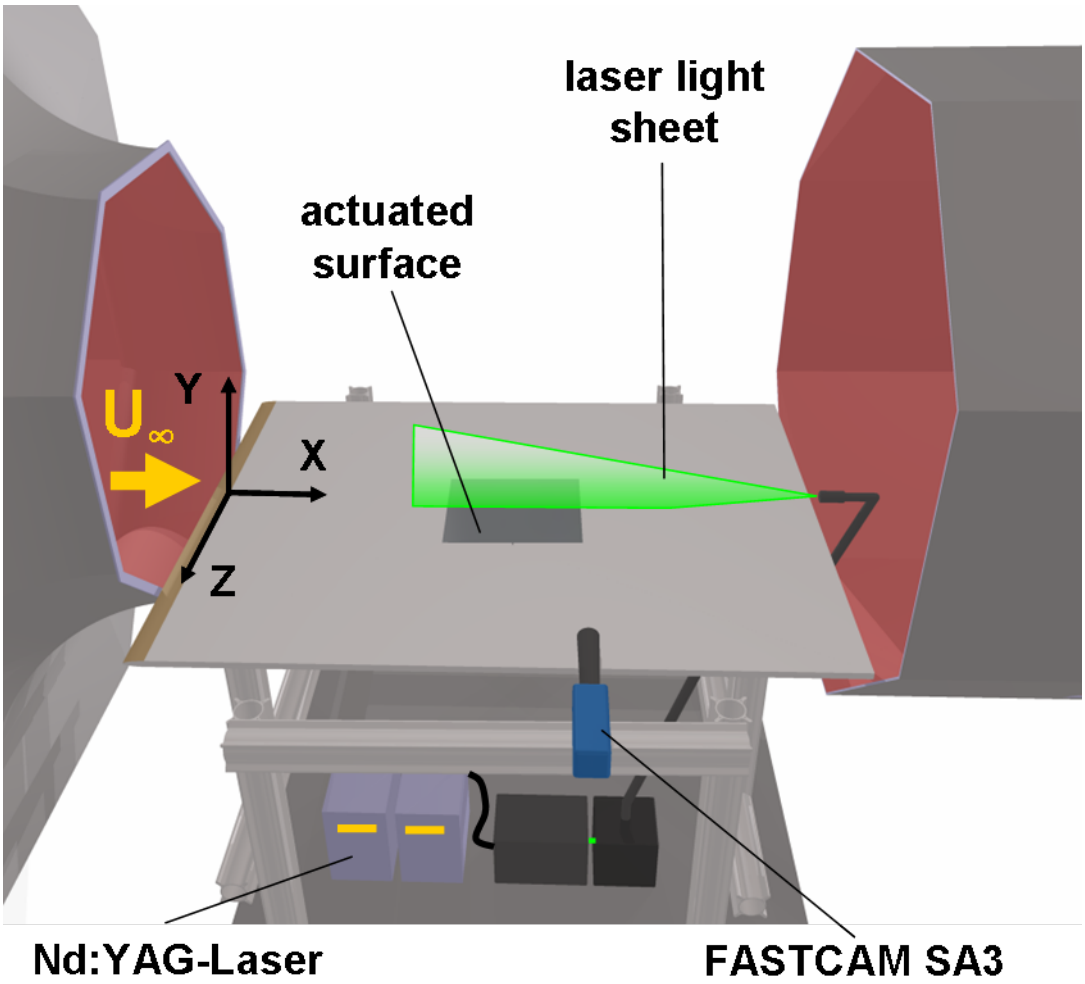

Figure 3.14: Sketch of the experimental setup showing the actuated surface and the PIV/μ-PTV arrangement.

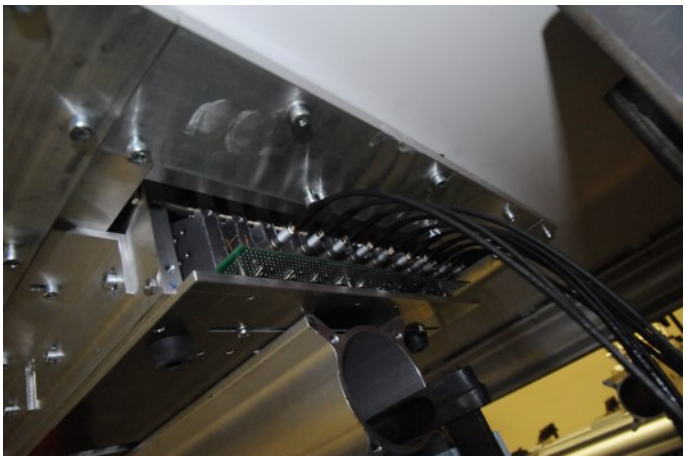

Figure 3.15: Actuating system mounted underneath the aluminum sheet.

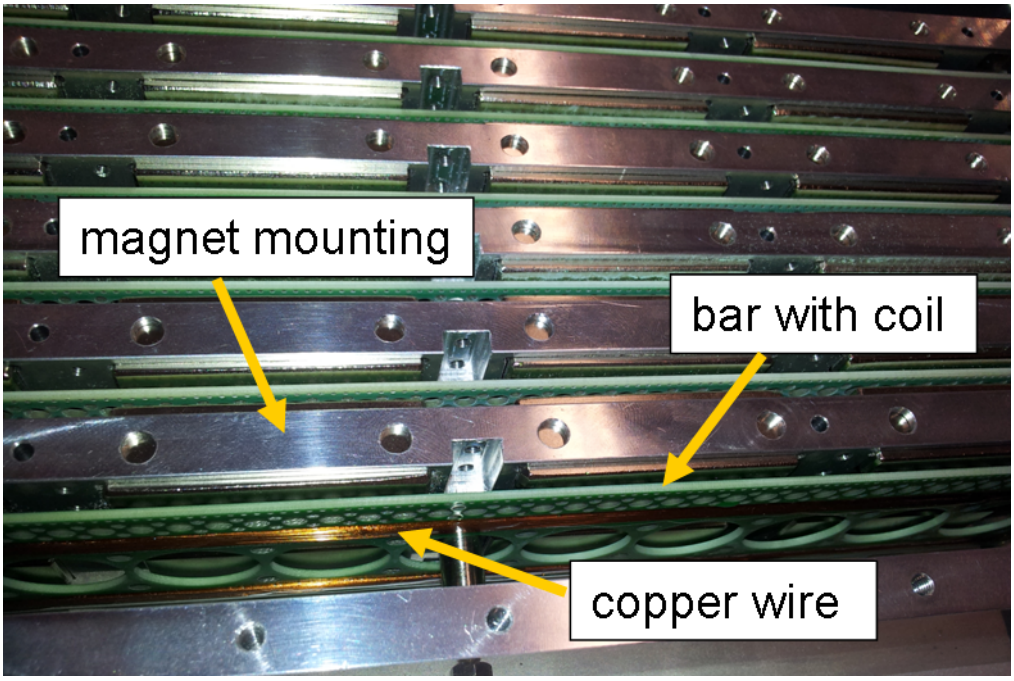

Figure 3.16: Electromagnetic actuating device.

Figure 3.17: Control unit of the actuating system.

PIV and μ-PTV measurements are conducted for three Reynolds numbers based on the freestream velocity and the momentum thickness immediately downstream of the actuated surface at a fixed wave length and frequency of the spanwise transversal wave. The dimensional flow quantities and the corresponding non-dimensional flow parameters in inner wall units, i.e., T^+, λ^+ and A^+, are summarized in Table 3.1

Table 3.1: Flow parameters: the normalized parameters are defined in inner wall units by $T^+ = u_\tau^2/(f \cdot \nu)$, $\lambda^+ = \lambda \cdot u_\tau/\nu$, $A^+ = A \cdot u_\tau/\nu$, where the friction velocity u_τ is determined for the non-actuated surface and ν represents the kinematic viscosity.

Test parameter	**Parameter range**	**Normalized parameter range**
Velocity	$U_\infty = 8, 12$ and $16\,\mathrm{m\,s^{-1}}$	$Re_\theta = 1200, 1660$ and 2080
Excitation frequency	$f = 81\,\mathrm{Hz}$	$T^+ = 110, 230$ and 380
Wave length	$\lambda = 160\,\mathrm{mm}$	$\lambda^+ = 3862, 5563$ and 7170
Amplitude	$A = 0.25, 0.3$ and $0.375\,\mathrm{mm}$	$A^+ = 6$ – 17

3.3 Measurement techniques

The velocity field is measured by PIV and μ-PTV. These laser-optical, nonintrusive measurement techniques enable the planar measurement of unsteady flow fields. Unlike PIV, the PTV technique uses a lower concentration of particles that allows tracking the particles individually over two consecutive images. In the following, the PIV and PTV methods are briefly described. To determine the velocity distribution over the complete boundary layer thickness, the standard 2D PIV technique is used. As seen on the schematics of Figure 3.18, the measurement planes are located directly downstream of the moving surface parallel to the mean flow and normal to the surface of the flat plate with a measurement area of $30 \times 30\,\mathrm{mm}^2$. This arrangement is used to determine the streamwise velocity field. When measuring the spanwise velocity field, the camera and mirror swap positions. To determine the wall-shear stress distribution, the velocity profile in the viscous sublayer has to be resolved. Since the viscous sublayer thickness is about $0.2\,\mathrm{mm}$ $(y^+ = 5)$ at a free stream velocity of $8\,\mathrm{m/s}$ and $0.86\,\mathrm{m}$ downstream of the leading edge, a high resolution measurement system like μ-PTV has to be applied. A long distance microscope is used to capture a measurement area of $2 \times 2\,\mathrm{mm}^2$. Due to the low particle density in the near wall region, it is necessary to use particle tracking algorithms instead of standard PIV cross-correlation techniques.

The `Photron FASTCAM SA3` camera is used for both methods. It has a resolution of 1024×1024 pixels and a CMOS sensor with a dynamic range of 12 bit. To increase the resolution, the `Infinity`$^{\mathrm{TM}}$ `K2`® model long-distance microscope (Figure 3.19) equipped with the `Standard`

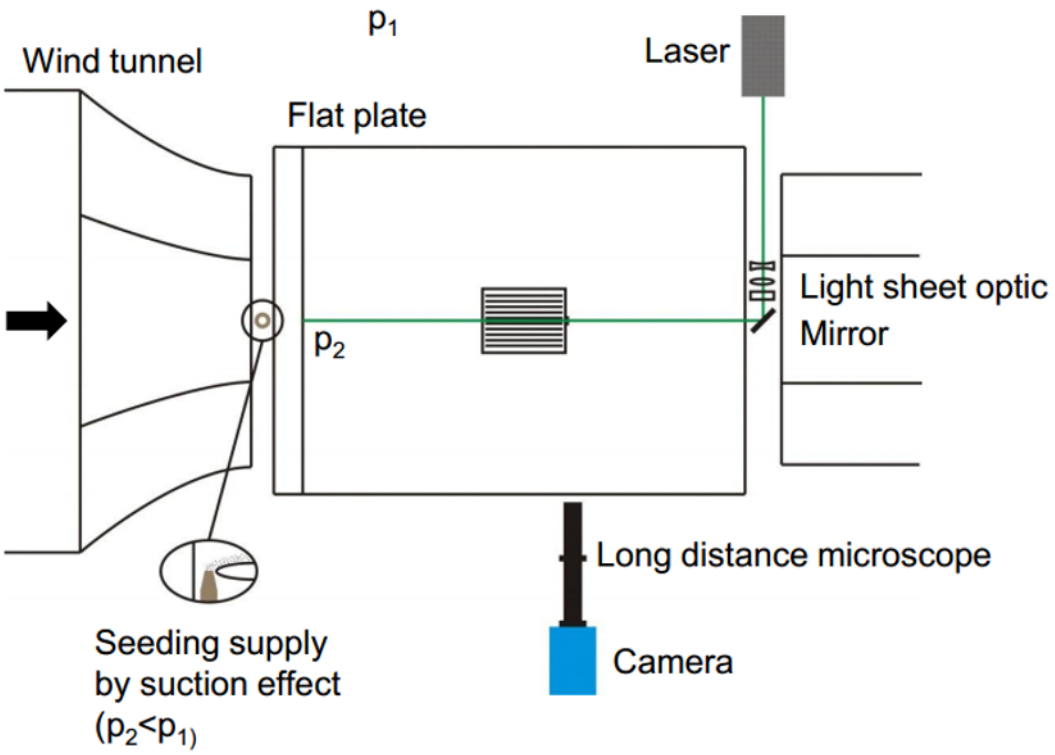

Figure 3.18: Schematics of the µ-PTV setup showing the Δp-induced suction effect.

`Objective` is coupled with the `FASTCAM SA3` camera. This camera-microscope set is mounted on a column whose height is adjustable through an hydraulic motor. The fine tuning of the camera's position is achieved by a transverse adjustable in three axial directions. To enable a clear field of view by the camera, the column is tilted 0.5° towards the table. The software `Camware®` is used to control the camera and download its recordings. Before each measurement, a calibration standard which has a micro-metric grid imprinted on it is positioned on the target area. Then, a picture of it is taken by `Camware®` in order to generate the calibration function with `PIVmap®`, by manually positioning the digital grid points over the points of intersection of the recorded grid pattern.

The light sheet with a thickness of 0.5 mm is generated by a double pulsed neodymium-doped

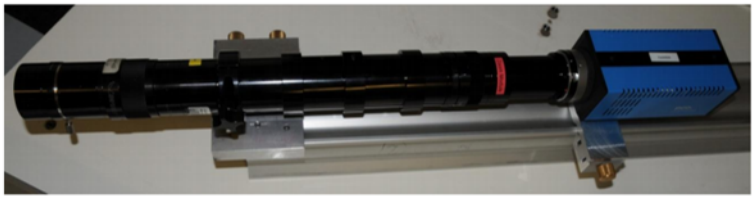

Figure 3.19: Long distance microscope

yttrium aluminium garnet (ND:YAG) Q-Switched Laser, manufactured by `Quanted Twins BSL 140`, with a wavelength of $\lambda = 532\,\text{nm}$ and a maximum energy per pulse of 140 mJ. The cameras and the light sheet are controlled by an external synchronizer operated at a double pulse frequency of 25 Hz.

In the specific setup of this work the laser sheet is produced as explained in section 3.1. However, to keep the working field flexible, the height of the sheet is made constant and the thickness is kept small. Attempts to reflect the laser light with only one mirror turned out to be unacceptable concerning the sheet thickness and therefore energy density. A laser arm is used instead to first point the light in the right direction and then produce the sheet with the optics. This allows for only the optics to be needed in precise position, instead of the whole laser. The arm is an articulated mirror arm manufactured by ILA. The laser sheet optics, also by ILA, are mounted on a rail which is mounted on a three-axis traverse similar to that of the camera to enable fine positioning. In this setup the laser goes from the downstream to the upstream end of the table.

For the PIV measurements the tunnel flow is seeded with di-ethyl-hexyl-sebacat (DEHS) particles with a mean diameter of 2-4 µm. This size is ensured by an impactor plate. The particles are produced by a seeding generator that incorporates an impactor plate with the required hole diameter, and then added to the flow in the diffuser of the wind tunnel.

At µ-PTV measurements, the particle distribution has to be intensified in the near wall region. To ensure a sufficient particle distribution close to the wall, a seeding nozzle is mounted 200 mm upstream of the leading edge of the flat plate. Investigations showed that this distance to the leading edge is necessary to avoid any influence on the near wall flow field. The particles are not injected but sucked into the flow field from a plastic container serving as plenum that contains air at a high particle concentration. The air flowing over the nozzle causes a vacuum based on Bernoulli's principle, causing the particles to be sucked out of the plenum into the flow.

For each configuration, 1362 image pairs are acquired by the PIV technique and 6810 for the µ-PTV measurements, which after post-processing are temporally averaged to obtain the final velocity data. To determine the flow field, the PIV data are evaluated using the commercial `PIVview®` software. The interrogation window size has 24×24 pixels with an overlap of 50%, which allows a spatial resolution of the measurement of $0.364 \times 0.364\,\text{mm}^2$ $(y^+ = 8.4)$. Each instantaneous vector field consists of 84×84 vectors, which generates 7056 data points. The `PIVview®` software uses an iterative interrogation method with a subpixel window shift and a Gaussian peak fit estimator. For subpixel shift, a third-order Beziél spline interpolation is applied. Furthermore, a dewarp function in the `PIVmap®` software is applied to the images, to reduce distortion caused by the optical systems. The recorded size of the seeding particles is 2-3 pixels. Contrast enhancement is used for preprocessing, to minimize the influence of the laser light reflections close to the wall. The cross-correlation results of the measurements indicate in their instantaneous vector fields less than 0.2% erroneous vectors. These erroneous vectors are detected in the postprocessing step using a normalized median test over 3×3 vectors according to Westerwell and Scarano [22] and are replaced by interpolated vectors.

The PTV data are analysed using a Matlab® routine based on a IDL-Code of Crocker and Grier

[23]. The images are filtered by a spatial bandpass filter smoothing the image and subtracting the background. Subsequently, the centroids of the bright particles are calculated to sub-pixel accuracy. Finally, the displacement of each particle per image pair is determined by a tracking algorithm. To average data, the images are divided into intervals parallel to the wall of 10 µm ($0.24 < y^+ < 0.45$) height. The velocity vectors of each interval are averaged over all image pairs. Thus, the resulting mean values show the velocity profile in the near-wall region.

3.4 Experimental uncertainties

The friction velocity u_τ is frequently used to normalize the velocity profiles. In this work, it is calculated by a least squares linear fitting in the viscous sublayer ($y^+ < 5$), using the linear relationship $u = y \cdot u_\tau^2/\nu$, that comes from observing that $u^+ = y^+$ in that region. The uncertainty that the value of u_τ calculated through this method carries onto the derived results such as the wall stresses τ_w, the friction coefficients c_f, and ultimately the drag reduction DR has to be determined. This uncertainty, although initially stemming from randomness, becomes a systematic error since it is propagated onto the final derived results.

In Appendix B, a methodology for calculating the uncertainty of the final result U_{DR} due to the uncertainty of u_τ determined with the aforementioned regression is proposed.

Restating the assumption that in the viscous sublayer ($y^+ < 5$) the mean velocity profile has a linear relationship in non-dimensional form $u^+ = y^+$ which translates to $u = y \cdot u_\tau^2/\nu$ in the dimensional form, then the relative systematic error, shortly referred as bias, associated with u, B_u/u, is given by

$$\left(\frac{B_u}{u}\right)^2 = \left(\frac{B_y}{y}\right)^2 + \left(\frac{B_\nu}{\nu}\right)^2 + 4 \cdot \left(\frac{B_{u_\tau}}{u_\tau}\right)^2 \tag{3.3}$$

Since data measured for $y^+ < 5$ are retrieved through µ-PTV, the uncertainty associated with this technique is first analyzed. The accuracy of particle-tracking methods depends on the ratio between the particle spacing in one image Δx_p and the particle displacement between images of an image pair Δx. Maas et al. [24] determined that $\Delta x_p = 5\Delta x$ results in almost 100% valid links between particles for synthetic particle images. With a mean particle spacing of $\Delta x_p = 145$ pixels and a maximum particle displacement of $\Delta x = 20$ pixels in the current measurements this condition is fulfilled. The bias component that pertains to the viscosity is so small compared to the others than it can be regarded as nil. As for the component B_y/y associated with the wall-normal coordinate, y, one has to consider the limitations of manually positioning a series of digital grid points over a picture taken of the calibration grid. This is done with the pre-processing software PIVmap®. Even though the software possesses some detection routines, enabling a faster positioning of those points, the final adjustments are made by the user. Finally, the component B_{u_τ}/u_τ is related to the least square linear fitting used to determine the friction velocity in the viscous sublayer.

As for PIV data, according to Westerweel [25] the typical value for the bias is about 0.1 pixel. In the current PIV experiments, the particle displacement measurements outside the boundary layer at $u_\infty = 8\,\text{m/s}$, 12 m/s and 16 m/s reach values of 9 pixels that lead to a relative systematic error of about 1%. Considering the same sequence of parameters inside the boundary layer close to the wall, the velocity has a value of about 4 m/s, 6 m/s and 8 m/s such that the particle displacement decreases to 5 pixels resulting in a relative systematic error of about 2%. Velocity vectors close to the wall are not recorded since only the interrogation windows, which are completely covered by the boundary layer flow, are accepted for computation of the correlation. Thus, the near-wall region, i.e., the region below 0.7 mm, is not considered in the PIV results.

We now consider the relative random error of the measured velocity, $\frac{P_u}{u}$. Also according to Westerweel [25], a typical value for the random error in the routines of the PIV measurements is 0.05 - 0.1 pixel. Experimental investigations with similar interpolation schemes by Lecordier and Trinité [26] achieved a minimum error of 0.044 pixels. Following Benedict and Gould [27], the variance of the mean velocity component is given by $\text{var}(\overline{u}) = \overline{u'^2}/N$. The theoretical random error of the mean velocity $\overline{u}$ on a 95% confidence interval is $\Delta u = 1.96\sqrt{\text{var}(\overline{u})}$. Considering the number of samples $N = 1362$, the maximum random error based on $\overline{u}$ of the PIV data is 1.3%. For the µ-PTV data, the maximum random error is 1.2% in the near-wall region $y^+ < 15$. In the region $y^+ > 15$, it is less than 0.8%.

Combining both relative systematic and random error, we get the total relative uncertainty, given by:

$$\left(\frac{U_{u^+}}{u^+}\right)^2 = \left(\frac{B_{u^+}}{u^+}\right)^2 + \left(\frac{P_{u^+}}{u^+}\right)^2. \tag{3.4}$$

3.5 Vortex counting through swirling strength

To better ascertain the nature of a turbulent flow, it is possible to complement a traditional analysis based in the velocity profile in the near-wall flow with a quantitative description of vortical structures, taking benefit of the immense numerical data obtained from PIV measurements. Making use of measurements taken in target areas parallel or perpendicular to the flowstream direction, the detection of spanwise and streamwise vortices can be made, respectively. We therefore ask the reader to indulge in the following reasoning, starting with a quote of Adrian et al. [28]:

> "In three dimensions, the local velocity gradient tensor will have one real eigenvalue (λ_r) and a pair of complex conjugate eigenvalues ($\lambda_\text{cr} \pm i\lambda_\text{ci}$) when the discriminant of its characteristic equation is positive. When this is true, the particle trajectories about the eigenvector corresponding to λ_r exhibit a swirling, spiral motion [29]. λ_ci^{-1} represents the period required for a particle to swirl once about the λ_r-axis. If the flow is pure shear flow, the particle orbits are infinitely-long ellipses and the orbit period is also infinite, corresponding to $\lambda_\text{ci} = 0$. Thus, $\lambda_\text{ci} > 0$ corresponds to shorter, more circular ellipses, i.e. eddies."

Because PIV fields are usually two-dimensional, the full local velocity gradient tensor cannot be formed. However, an equivalent two-dimensional form of this tensor can be computed in the plane in which the PIV data lies [28], and be written in matrix form as:

$$(\nabla \mathbf{u})_{2\text{-}D} = \begin{pmatrix} \frac{\partial u}{\partial x} & \frac{\partial u}{\partial y} \\ \frac{\partial v}{\partial x} & \frac{\partial v}{\partial y} \end{pmatrix} \tag{3.5}$$

This tensor will either have two real eigenvalues or a pair of complex conjugate eigenvalues. In the latter case, the absolute value of imaginary component is called *swirling strength*, λ_{ci}, as its magnitude indicates how prevalent is the local swirling motion, associated with the presence of vortices, as referred in the paper of Adrian and colleagues [28]. Such finding had already been made by Zhou et al [30, 31]. In order to retrieve the direction of this swirling motion, a modified swirling strength parameter is introduced, Λ_{ci}, taking into account the sign of the vorticity measured perpendicular to the flow stream, ω_z:

$$\Lambda_{ci}(x,y) \equiv \lambda_{ci}(x,y) \frac{\omega_z(x,y)}{|\omega_z(x,y)|} \tag{3.6}$$

A new scalar-field property, Λ_{ci}, can be computed using Matlab® routines for the whole measured field and represented in contour plots with Tecplot®. A further step can be taken by removing the in-homogeneity of the flow in the wall-normal direction with respect to swirling strength by introducing a threshold value of $1.5 \cdot \lambda_{ci}^{rms}(y)$ at each wall-normal location [32].[1] In this work, Λ_{ci} is normalized as $\Lambda_{ci}/\Lambda_{ci}^{rms}(y)$ with the threshold working as follows: when $\Lambda_{ci}/\Lambda_{ci}^{rms}(y) > 1.5$, $\Lambda_{ci}/\Lambda_{ci}^{rms}(y)$ retains its value; otherwise, it is set to zero. The use of this threshold value conditions the identification of the boundaries of the vortex regions. Wu and Christensen [33] first tried using a threshold of $1.0 \cdot \lambda_{ci}^{rms}(y)$ but the vortex sections came with very jagged edges, indicating contamination by the experimental noise associated with differentiation of the PIV data, which alters the space occupied by the cores. Setting a slightly larger threshold, such as $1.5 \cdot \lambda_{ci}^{rms}(y)$, limited the influence of experimental noise that accompanies the calculation of $\nabla \mathbf{u}$ from PIV measurements.

While useful in giving a qualitative visual description at a particular time-step, these Λ_{ci}-contour plots do not suffice in terms of quantitatively describing a whole data set retrieved from turbulent flow conditions. For a comparative analysis in terms of changes in flow structures between the four cases, non-actuated and three others with varying amplitude studied, a proper vortex counting method based on the modified swirling parameter has to be applied. Employing the procedures outlined by Lee and Choi in [32], the population trends of negative (clockwise or prograde) and positive (counterclockwise or retrograde) spanwise vortices are obtained as a function of the wall-normal direction (y), by spatially averaging the count of vortices over a rectangular area of wall-normal height $3\Delta y$, where $3\Delta y$ represents the distance between adjacent vertical grid

[1] Since λ_{ci} is highly intermittent because it is non-zero only within vortex cores, the mean of λ_{ci} is extremely small compared to its rms value. As such $\Lambda_{ci}^{rms}(y)$ is representative of the characteristic magnitude of Λ_{ci} within vortices at a given y. [33]

points, and length L_x equal to the horizontal length of the field of view. The population is then described by taking the temporal mean of a specific data-set:

$$\Pi_{\mathrm{n(p)}}(y) = \frac{1}{3}\sum_{3\Delta y}\sum_{L_x} \text{number of negative (positive) vortex centers.} \tag{3.7}$$

This quantity can be normalized, that is scaled in wall-units, by dividing the aforementioned count by the considered area, which yields a *vortex population density*:

$$\Pi^{+}_{\mathrm{n(p)}}(y) = \frac{\Pi_{\mathrm{n(p)}}(y)}{\frac{\Delta y\, u_\tau}{\nu}\frac{L_x\, u_\tau}{\nu}} \tag{3.8}$$

Using a height of $3\Delta y$ in the averaging window decreases scatter in the population curves, as referred by Wu and Christensen [33].

Chapter 4

Results and Discussion

In the following, the impact of the spanwise transversal wave on the wall-shear stress distribution is investigated by juxtaposing near-wall velocity profiles for the actuated and the non-actuated surface. In a first instance, the freestream Reynolds number and the wave length and the frequency of the transversal wave are constant while the amplitude of the surface wave is increased, i.e. the perturbation imposed on the boundary layer is enlarged. Secondly, the influence of higher freestream Reynolds numbers is analyzed. Thirdly, the results are compared with the findings of Tamano and Itoh [34]. Finally, an analysis of the flow structure based on counting spanwise and streamwise vortical structures is presented.

4.1 Velocity profiles

Figure 4.1a shows the ensemble- and space-averaged[1] mean streamwise velocity profiles of the turbulent boundary layer for the three surface-actuated, or moving cases, comparing each to the surface-non-actuated, or non-moving case. The velocity is scaled by the friction velocity u_τ of the non-actuated configuration for a freestream velocity of $8\,\mathrm{m\,s^{-1}}$. The data are measured 2 mm downstream of the surface that is actuated by a frequency of 81 Hz. In inner wall units the frequency is $T^+ = u_\tau^2/(f \cdot \nu) = 110$, the wave length $\lambda^+ = \lambda \cdot u_\tau/\nu = 3862$, and the amplitude $A^+ = A \cdot u_\tau/\nu = 6$. The corresponding Reynolds number based on the freestream velocity and momentum thickness at the measurement location is $Re_\theta = 1200$. The friction velocity $u_\tau = 0.364\,\mathrm{m\,s^{-1}}$ is determined by a least square linear fitting in the viscous sublayer ($y^+ < 5$). To analyze the impact of the actuation over the entire boundary-layer thickness, the PIV and µ-PTV data are combined such that one single smooth distribution is shown. The overlap of both measurement techniques covers the region $12 < y^+ < 22$. The match of the curves evidences the convincing agreement of the results of both measurement techniques.

At a first glance, there seems to be hardly any difference between the actuated and non-actuated configurations visible in the viscous layer, where the measurements match the linear increase of the

[1] For each time-step and wall-normal location, a spatial average of the velocity is performed over an horizontal line stretching the length of the field of view, but excluding outlier edge grid points. The final mean is then computed by ensemble-averaging those spatial averages through all time-steps.

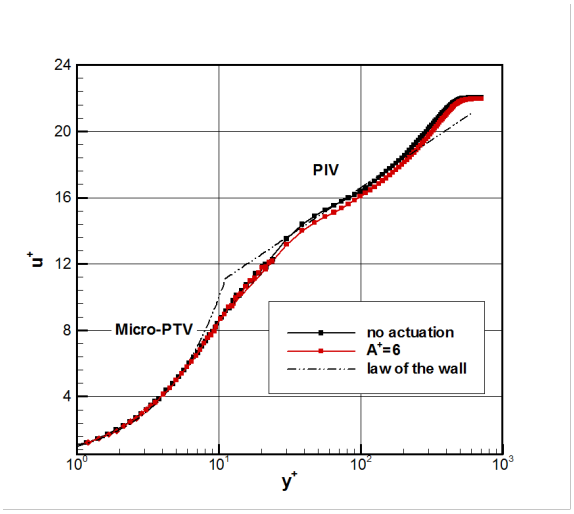

(a)

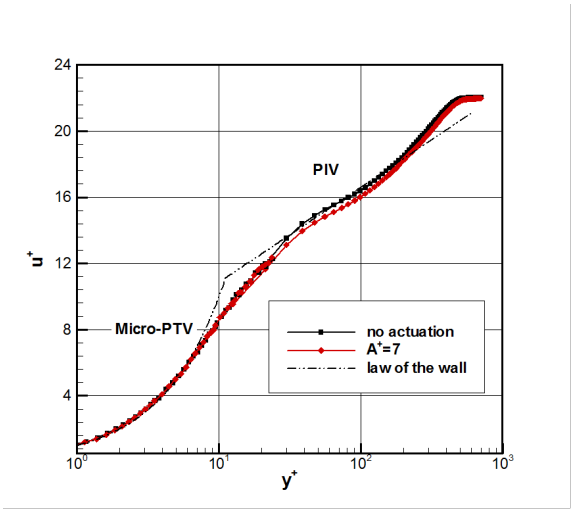

(b)

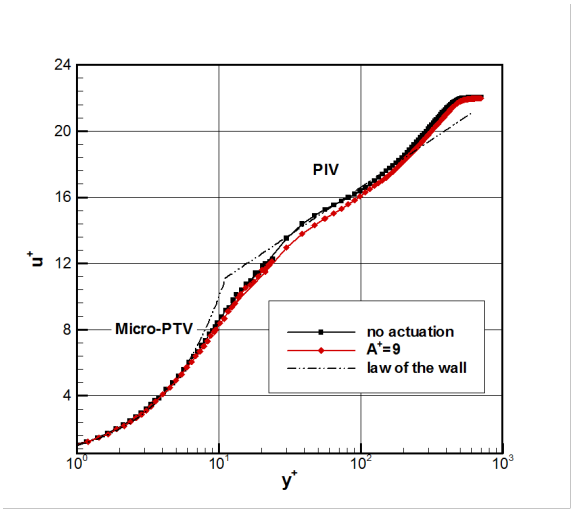

(c)

Figure 4.1: Comparison of the mean streamwise velocity distributions downstream of the actuated area for $Re_\theta = 1200$, $T^+ = 110$, $\lambda^+ = 3862$, and (a) $A^+ = 6$, (b) $A^+ = 7$, and (c) $A^+ = 9$; inner wall units are defined by the friction velocity u_τ of the non-actuated surface.

velocity distribution. For $y^+ > 30$, the effect of the actuation is indicated by slightly lower velocity values in the logarithmic region for the actuated configuration, reaching a maximum deviation of about 2.9% at $y^+ = 40$.

Increasing the amplitude to $A^+ = 7$ and keeping Re_θ, T^+, and λ^+ constant confirms that primarily the outer turbulent boundary layer is affected by the spanwise traveling wave, as observable in Figure 4.1b. A further increase of the amplitude to $A^+ = 9$, Figure 4.1c, generates lower velocities of approximately 4.4% in the logarithmic region for the actuated configuration while hardly any influence on the velocity distribution in the viscous sublayer can be detected.

To evidence the impact of the actuation and the increasing amplitude on the near-wall flow field, the mean velocity profiles of the $A^+ = 6$, 7 and 9 configurations are plotted in Figure 4.2 in linear scaling. The enlargement of the viscous sublayer $(y^+ < 5)$ clearly shows lower gradients for all actuated cases compared with the non-actuated configuration confirming a reduction of the friction drag. Using the wall shear stress τ_w determined by

$$\tau_w = \mu \frac{\partial u}{\partial y}\bigg|_{y=0} \approx \mu \frac{du}{dy}\bigg|_{y=0} \tag{4.1}$$

the drag-reduction ratio DR is calculated by the skin-friction coefficient $c_f = \tau_w / \left(1/2 \cdot \rho \cdot u_\infty^2\right)$:

$$\mathrm{DR} = \left(1 - \frac{c_{f,\mathrm{actuated}}}{c_{f,\mathrm{non-actuated}}}\right) \times 100\%. \tag{4.2}$$

The results evidence a reduction of the friction for all three actuation amplitudes ranging from DR = 2% for $A^+ = 6$ to a maximum value of DR = 3.42% for $A^+ = 9$.

At higher Reynolds number, i.e. $Re_\theta = 1660$ and $Re_\theta = 2080$ and constant dimensional frequency and wave length, the intricacy of the interaction of the near-wall turbulent flow and the transversal traveling wave becomes more evident. In Figure 4.3a the mean streamwise velocity distributions for $Re_\theta = 1660$ of the non-actuated and the actuated configurations at three amplitudes $A^+ = 9$, $A^+ = 10$, and $A^+ = 13$ are compared. Like for the lower Reynolds number, the influence of the actuated wall is only visible in the logarithmic region. The difference to the non-actuated wall decreases to a maximum value of about 1.1% at $y+ = 40$ for the highest considered amplitude $A^+ = 13$. Figure 4.3b shows the corresponding mean velocity distribution for the highest investigated Reynolds number $Re_\tau = 2080$ at $A^+ = 11$, $A^+ = 14$, and $A^+ = 17$. The influence of the actuation is no longer visible in the logarithmic region and the profiles of all configurations match the law of the wall.

The velocity distribution in the viscous sublayer in linear scaling in Figure 4.4 also indicates nearly no influence on the velocity gradients, i.e. the wall-shear stress for both Reynolds numbers. The maximum drag reduction is below 2%. At $Re_\theta = 2080$ a tendency towards a drag increase is observed.

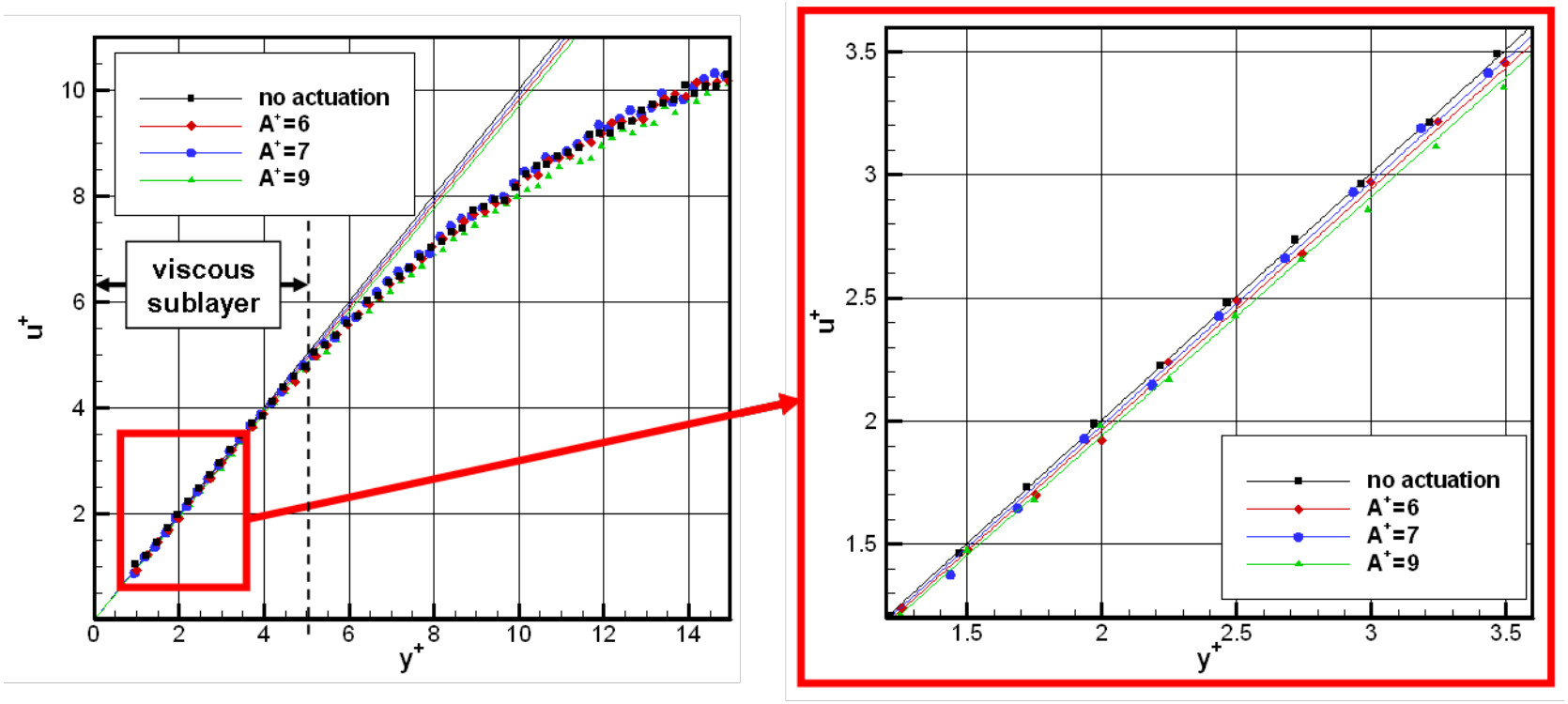

Figure 4.2: Comparison of the mean streamwise velocity in the viscous sublayer for the $Re_\theta = 1200$ flat plate flow actuated at $T^+ = 110$, $\lambda^+ = 3862$, and $A^+ = 6$, 7, and 9 with the non-actuated case; inner wall units are defined by the friction velocity u_τ of the non-actuated surface.

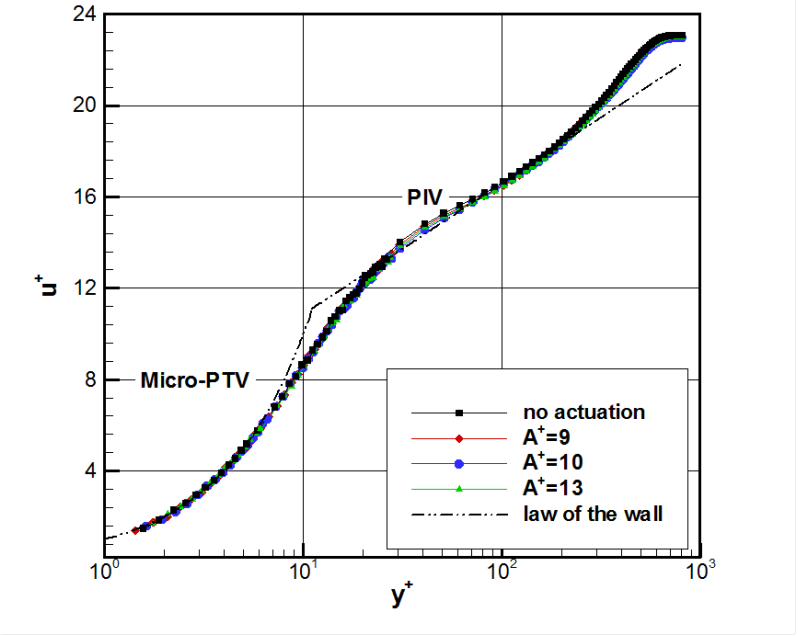

(a)

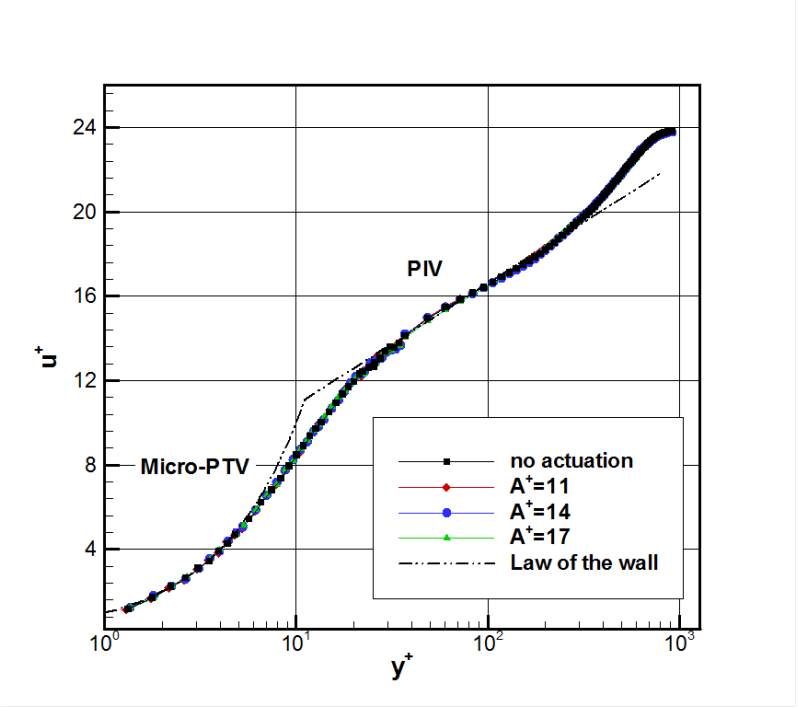

(b)

Figure 4.3: Comparison of the mean streamwise velocity distributions downstream of the actuated surface for (a) $Re_\theta = 1660$ and (b) $Re_\theta = 2080$ with the non-actuated configuration; three actuation amplitudes are considered; the dimensional frequency and wave length match the $Re_\theta = 1200$ case values; inner wall units are defined by the friction velocity u_τ of the non-actuated surface.

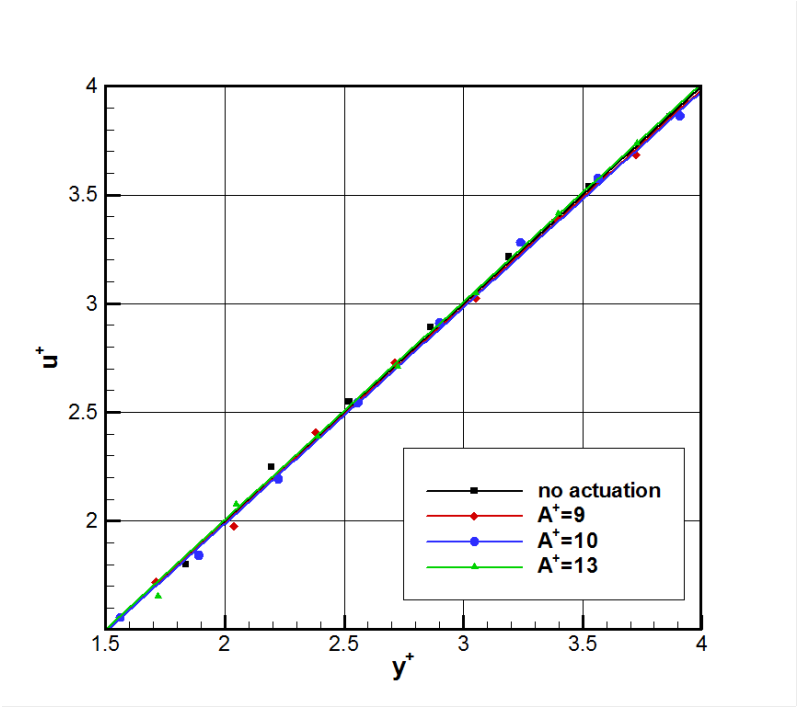

(a)

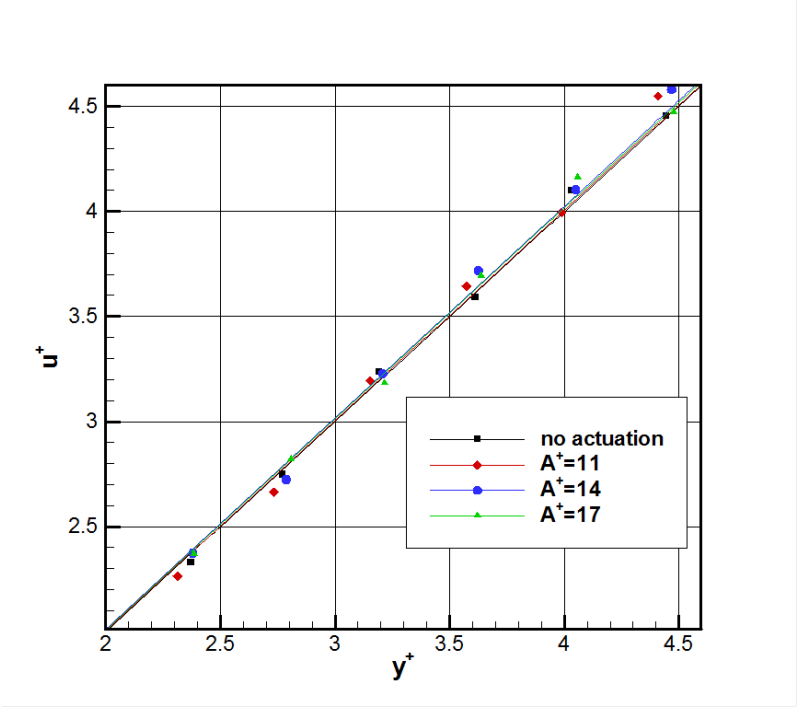

(b)

Figure 4.4: Comparison of the mean streamwise velocity in the viscous sublayer for the actuated and non-actuated flat plate; (a) $Re_\theta = 1660$, $A^+ = 9$, 10 and 13; (b) $Re_\theta = 2080$, $A^+ = 11$, 14 and 17; the dimensional frequency and wave length match the $Re_\theta = 1200$ case values; inner wall units are defined by the friction velocity u_τ of the non-actuated surface.

4.2 Root-mean-square value of velocity fluctuations

Figure 4.5 displays a comparison of the distributions of the root-mean-square value of the streamwise velocity fluctuations scaled by the friction velocity u_τ of the non-actuated wall of the lowest and highest Reynolds number flows. Note that the data are based on the PIV measurements. For the lower Reynolds number, $Re_\theta = 1200$, Figure 4.5a, the actuation increases the streamwise velocity fluctuations in the outer part of the turbulent boundary layer $(y^+ \geq 200)$ for all three actuated configurations compared with the non-actuated case. This tendency is no longer observed at $Re_\theta = 2080$, as seen in Figure 4.5b. That trend is similar to that shown with the mean velocity distribution in the logarithmic region seen in Figure 4.4b where the actuated data approach the non-actuated distributions. Also, the distributions of the root-mean-square value of the wall-normal velocity fluctuations illustrated in Figure 4.6 show the same behavior at varying Reynolds numbers. These results agree well with the findings by Tamano and Itoh [34] who also detected an increase of the velocity fluctuations in the outer boundary layer above the spanwisely actuated surface wave motion when an overall drag reduction was observed.

The results clearly show the influence of the surface wave motion on the turbulence distribution within the boundary layer. The higher velocity fluctuations above $y^+ = 100$ indicate a redistribution of the turbulence content away from the wall into the outer boundary layer. This redistribution leads to a reduction of the kinetic energy in the viscous sublayer resulting in a decrease of the wall-shear stress distribution.

4.3 Summary of velocity-related results

The summary of the results in Table 4.1 shows that an evident friction drag reduction is achieved for the lowest Reynolds number $Re_\theta = 1200$ and the highest amplitude $A^+ = 9$. Note that the dimensional actuation frequency and the wave length are kept constant. Unlike Tamano and Itoh [34], who determined the drag reduction by considering the growth rate of the momentum thickness, the wall-shear stress distribution is computed in this study to directly determine the skin-friction coefficient for the actuated and non-actuated configurations. For comparison, the DR values are plotted into an extended version of the diagram of Tamnho and Itoh [34], i.e. higher T^+ values are included, in Figure 4.7. The comparison confirms the findings of Tamano and Itoh [34] in the sense that at low T^+ values a drag reduction is achieved while at higher T^+ the drag reduction effect decreases. Note that Tamano and Itoh reached amplitude values of $A^+ = 30$ for $T^+ = 110$ which is higher than $A^+ = 9$ for $T^+ = 110$ in our measurements. Due to the more than threefold amplitude they achieve drag reductions up to 13%.

Careful interpretation of these results has to be observed, as a preliminary analysis of experimental uncertainty, such as that suggested in Appendix B, has revealed that the DR results carry an absolute error of approximately $\pm 4.5\%$, taking only into account the uncertainty yielded by determining the friction velocity u_τ with a least square linear fitting in the viscous sublayer.

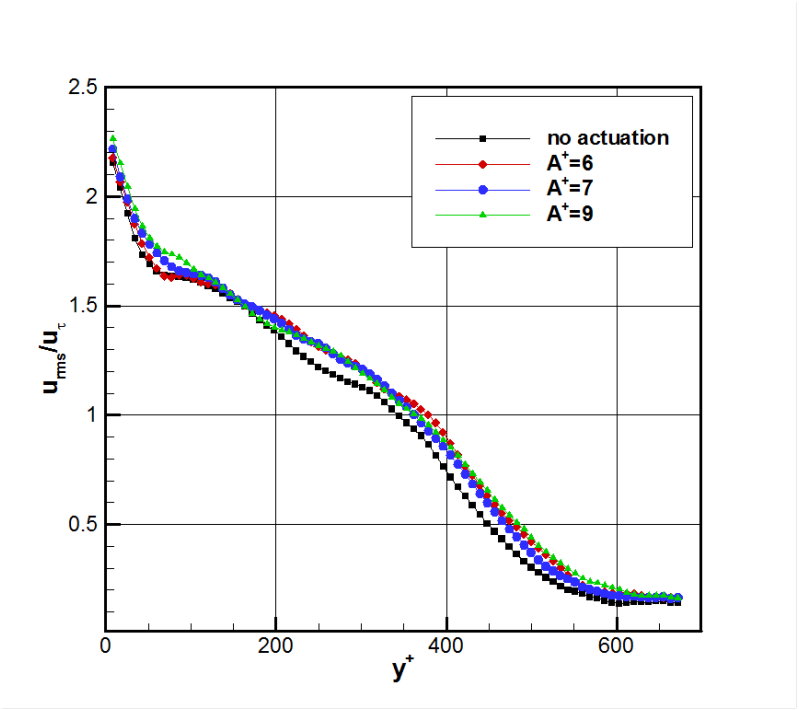

(a)

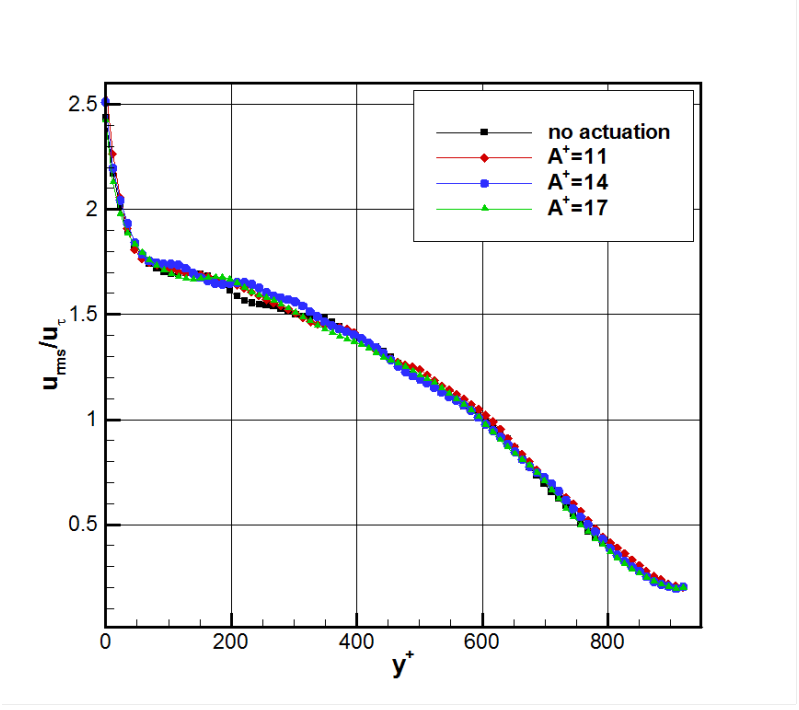

(b)

Figure 4.5: Comparison of the root-mean-square value of the streamwise velocity fluctuations scaled by the friction velocity u_τ of the non-actuated wall, downstream of the actuated wall, for the actuated and non-actuated surface; (a) $Re_\theta = 1200$, $A^+ = 6$, 7 and 9 (b) $Re_\theta = 2080$, $A^+ = 11$, 14 and 17; the dimensional frequency and wave length match the $Re_\theta = 1200$ case values; inner wall units are defined by the friction velocity u_τ of the non-actuated surface.

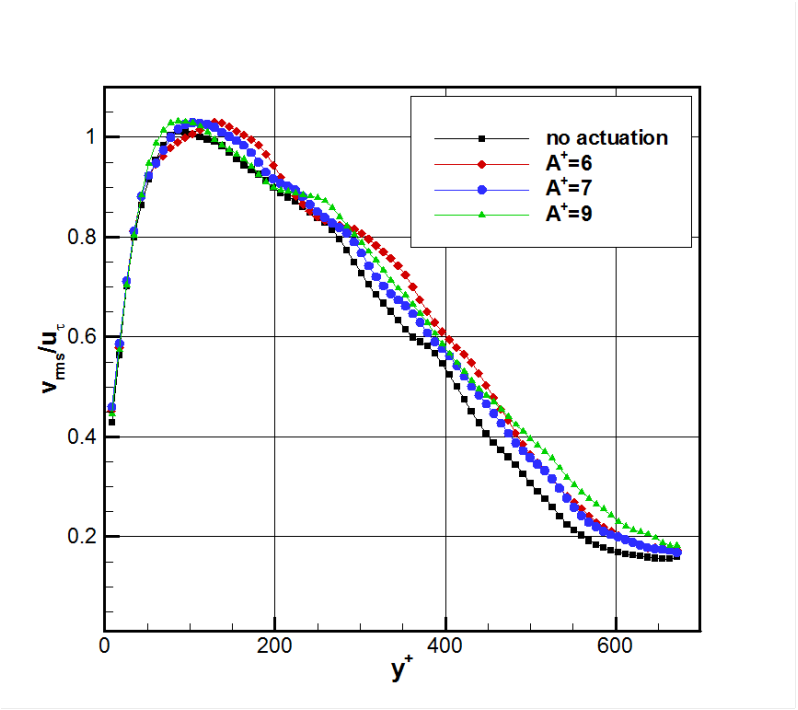

(a)

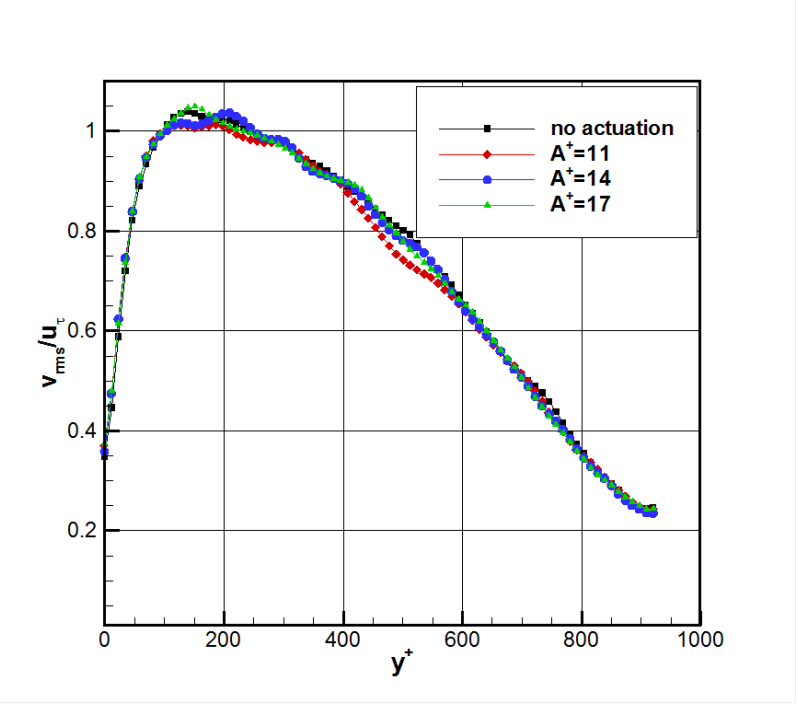

(b)

Figure 4.6: Comparison of the root-mean-square value of the streamwise velocity fluctuations scaled by the friction velocity u_τ of the non-actuated wall, downstream of the actuated wall, for the actuated and non-actuated surface; (a) $Re_\theta = 1200$, $A^+ = 6$, 7 and 9 (b) $Re_\theta = 2080$, $A^+ = 11$, 14 and 17; the dimensional frequency and wave length match the $Re_\theta = 1200$ case values; inner wall units are defined by the friction velocity u_τ of the non-actuated surface.

Table 4.1: Skin-friction coefficient c_f and drag ratio DR for the non-actuated flow and the actuated flat plate flows at three Reynolds number Re_θ and three wave amplitudes A^+; the dimensional frequency and wave length are constant; the normalized parameters are defined by $T^+ = u_\tau^2/(f \cdot \nu)$, $\lambda^+ = \lambda \cdot u_\tau/\nu$, and $A^+ = \cdot u_\tau/\nu$, where the friction velocity u_τ is determined for the non-actuated surface.

Re_θ	T^+	λ^+	A^+	c_f	DR [%]
1200	110	3862	0	0.00456	0.0
1200	110	3862	6	0.00447	2.0
1200	110	3862	7	0.00444	2.7
1200	110	3862	9	0.00440	3.4
1660	230	5563	0	0.00369	0.0
1660	230	5563	9	0.00367	0.4
1660	230	5563	10	0.00367	0.6
1660	230	5563	13	0.00370	-0.3
2080	380	7170	0	0.00322	0.0
2080	380	7170	11	0.00323	-0.4
2080	380	7170	14	0.00322	-0.2
2080	380	7170	17	0.00324	-0.7

4.4 Vortex identification and counting

For illustration purposes of the method followed, two contour plots are juxtaposed in Figure 4.8: one of the modified swirling strength parameter normalized by its RMS value and another of the same quantity but where the threshold of $\Lambda_{ci} > 1.5\Lambda_{ci}^{rms}$ has been applied. In other words, when $\Lambda_{ci}/\Lambda_{ci}^{rms} > 1.5$ then $\Lambda_{ci}/\Lambda_{ci}^{rms}$ retains its value. Otherwise, it is set to zero. In this way, the noise signal is filtered out and the vortical structures are better identified. The vectors of *modified velocity fluctuations* based on a local Galilean decomposition are overplotted solely within the vortical structures since they enhance the sense and direction of swirling motion already identified by $\Lambda_{ci}/\Lambda_{ci}^{rms}$. In short, a local velocity average is computed within the region of each vortical structure and then subtracted from the velocity measured in each grid point in that particular time-step to yield this modified velocity fluctuation.

These contour plots have been arbitrarily chosen from PIV data of the non-moving case with the target area parallel to the flow direction and $Re_\theta = 1200$, stored in the file associated with time-step number 50, and therefore represent a snapshot of the flow structure at that specific time. Picking data from a another time-step number or another moving/non-moving case for representation of these contour plots would only result in a different random arrangement of the flow structures to be shown, reflecting its turbulent nature.

One could argue that the vorticity maps could just as well evince the vortical structures. However, one can juxtapose a vorticity contour plot next to a $\Lambda_{ci}/\Lambda_{ci}^{rms}$ and, with benefit of hindsight, on both overplot the aforementioned modified velocity fluctuations. As seen in Figure 4.9, it is clear that the regions of non-zero vorticity do not necessarily match the regions where a vortex is present. This exercise can be repeated for u^+ and v^+, as presented in Figures 4.10

The results of the vortex identification counting technique explained in section 3.5, applied to target areas parallel to the flowstream, are presented in Figure 4.11. The flow conditions herein analyzed are a freestream velocity of $8\,\mathrm{m\,s^{-1}}$, corresponding to a $Re_\theta = 1200$. From a simple inspection, the number of vortices as function of the wall-normal coordinate is not perceived to suffer any alteration from the non-actuated to the actuated cases or, for that matter, change among the latter.

All curves seem to follow the same pattern: from the beginning till the middle of the buffer layer there is a sharp decrease in the population density of negative (clockwise or prograde) vortices, which fall from a count of 0.00010 at $y^+ \approx 120$ to approximately half of it at $y^+ \approx 140$, then experiencing a sudden increase to 0.00007 at $y^+ \approx 150$. From here till $y^+ \approx 200$ there is again a decrease to 0.00005 vortices. From then on, coming out of the inner layer and entering the outer layer at $y^+ \approx 300$, a quasi-steady decline is observable till reaching $y^+ \approx 650$ at a count of 0.00002 This trend is reversed from this point on, and a local maximum is observed at $y^+ \approx 800$ with the population density reaching 0.00004. Towards the end of the measured range, at $y^+ \approx 840$, the it declines again 0.00002.

As for positive (counterclockwise or retrograde) vortices, the curves of all four cases are practically coincident, starting with a population density 0 at $y^+ \approx 120$ and experiencing an increase of 0.00001 till reaching $y^+ \approx 200$, which defines a plateau for the next 100 wall units. In the region $300 < y^+ < 600$, the vortex population drops to 0.000005. Then, it rises up again to around 0.00004 at $y^+ \approx 800$, and hereinafter, as with the population density of positive, the same decrease is verified with 0.00002 being the popultion density observable at $y^+ \approx 840$.

Analyzing the data retrieved from measurements taken perpendicular to the flowstream, one can generate similar results on the counting of streamwise vortices. Because the curves of positive and negative vortex population densities versus y are similar and of difficult discernment when superimposed, these results are plotted in separate graphs, as seen in Figures 4.12 and 4.13. At first glance, the population densities are one order of magnitude larger than those of spanwise vortices. Moving from the non-actuated case to any of the actuated cases, there is an increase in the count of both prograde and retrograde streamwise vortices for $y^+ > 100$, inside the buffer layer. This increase seems to be slightly dependent on the amplitude A^+, since it is larger when $A^+ = 9$ compared to when $A^+ = 7$.

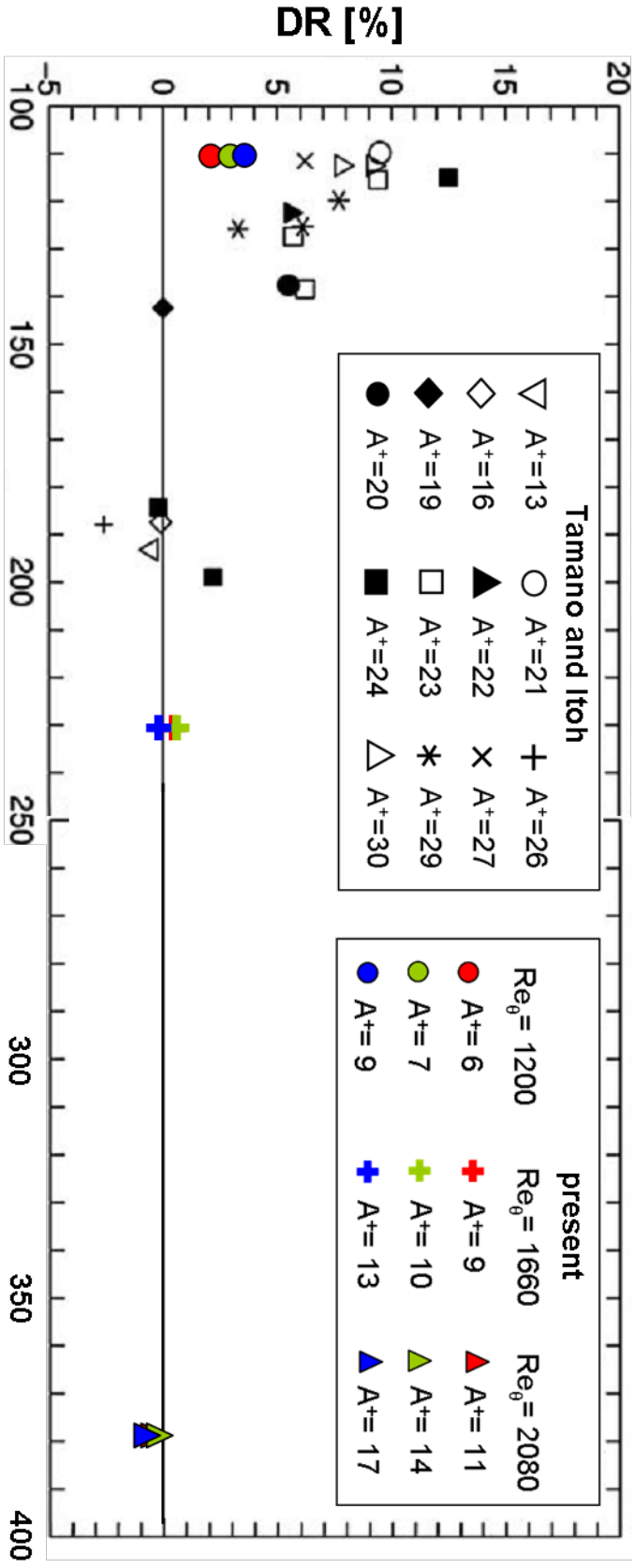

Figure 4.7: Extended diagram according to Tamano and Itoh [34] showing DR versus T^+.

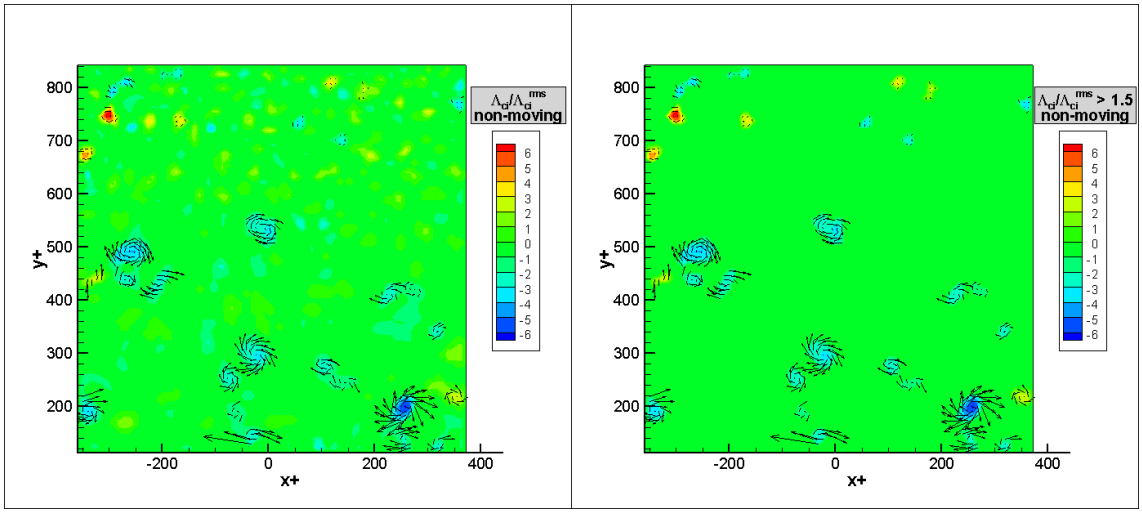

(a) Without threshold. (b) Applying threshold.

Figure 4.8: Contour plots of normalized modified swirling strength parameter, $\Lambda_{ci}/\Lambda_{ci}^{rms}$, from time-step no. 50, non-moving case, $Re_\theta = 1200$.

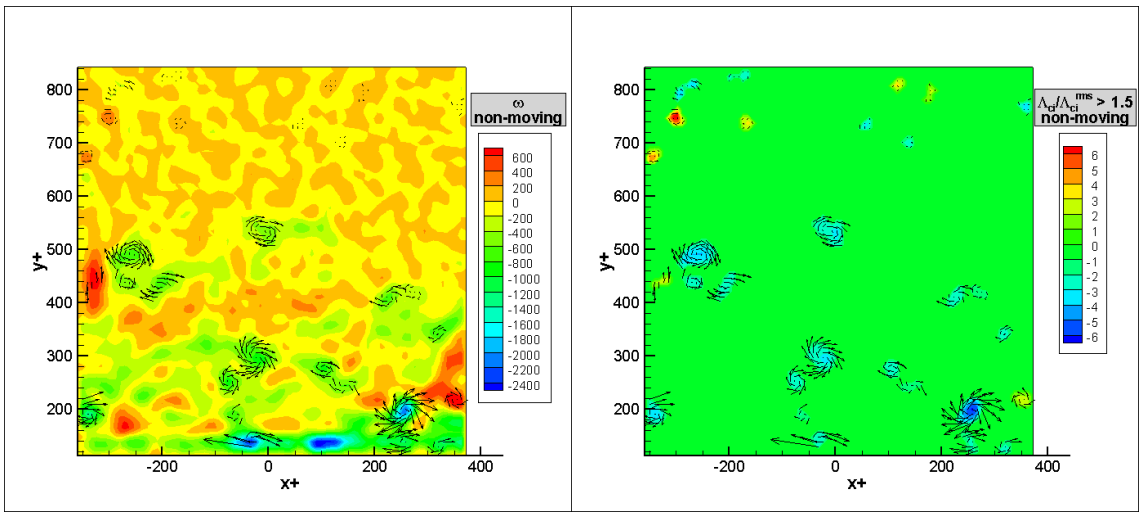

(a) Vorticity map. (b) $\Lambda_{ci}/\Lambda_{ci}^{rms}$

Figure 4.9: Contour plots of data from time-step no. 50, non-moving case, $Re_\theta = 1200$.

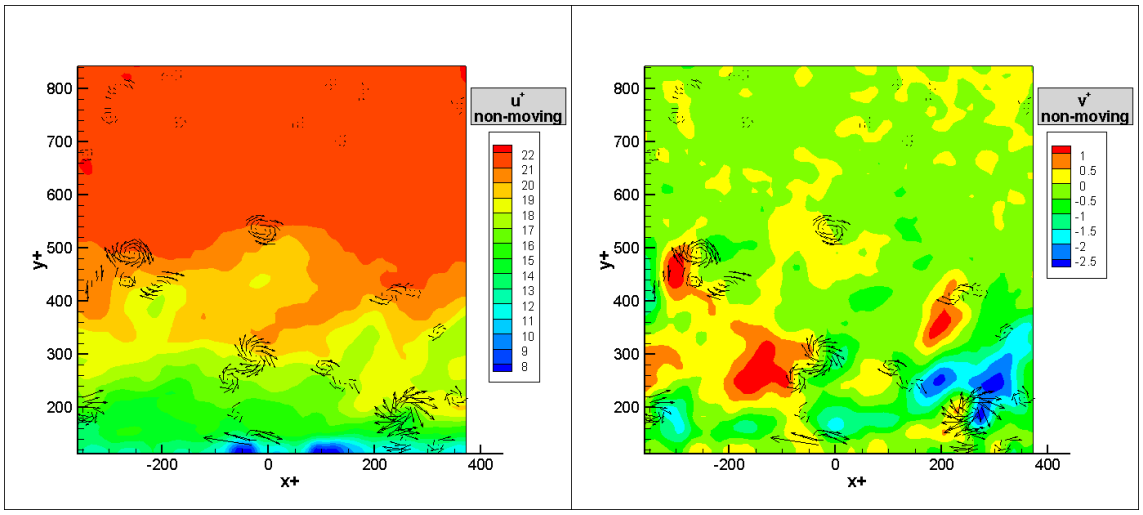

(a) Streamwise u^+ velocity component. (b) Wall-normal v^+ velocity component.

Figure 4.10: Contour plots of data from time-step no. 50, non-moving case, $Re_\theta = 1200$.

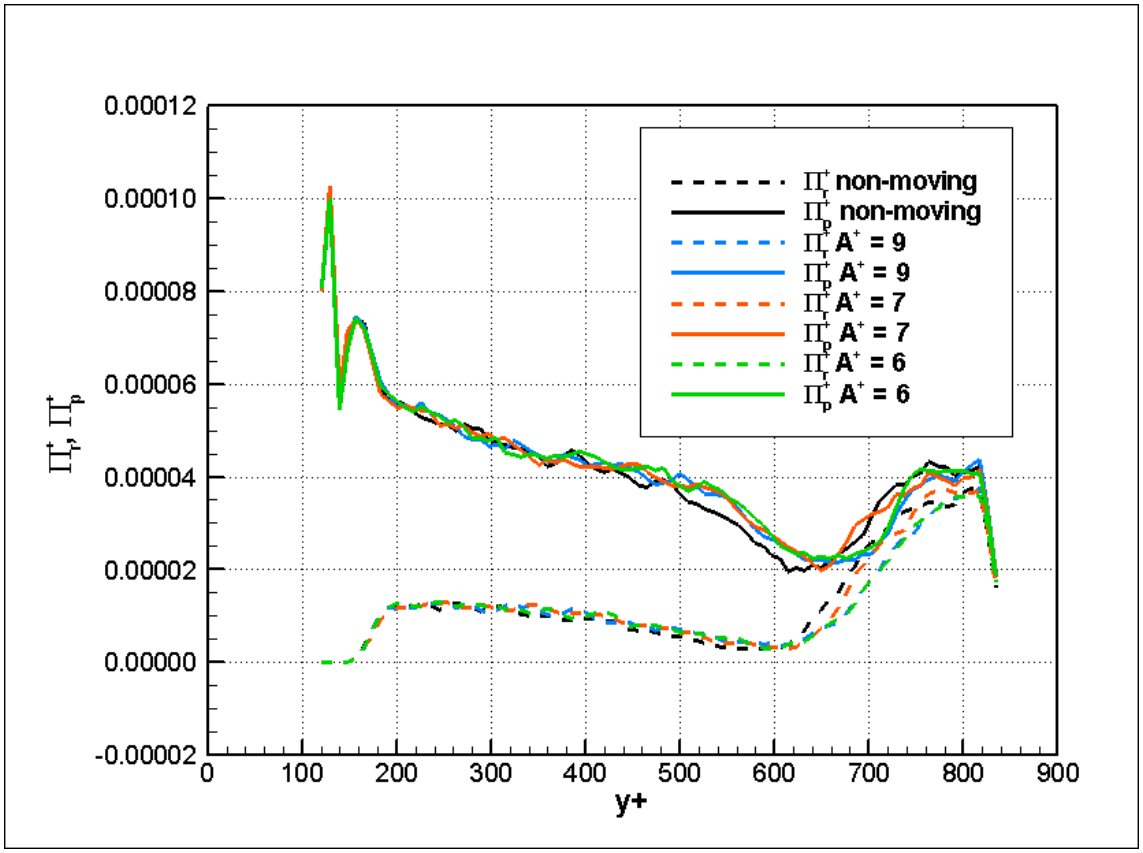

Figure 4.11: Spanwise positive (also named retrograde, Π_r) and negative (prograde, Π_p) vortex counting comparing four cases: non-actuated and three actuated cases, with varying amplitude. This counting refers to target areas parallel to the flowstream, with $Re_\theta = 1200$.

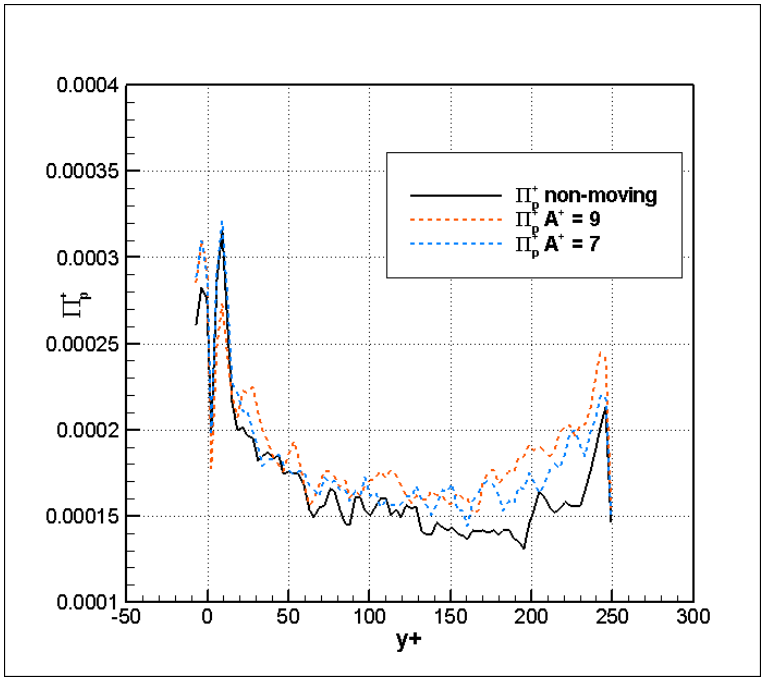

Figure 4.12: Streamwise negative $\left(\text{prograde}, \Pi_p\right)$ vortex counting comparing three cases: non-actuated and two actuated cases, with varying amplitude. This counting refers to target areas perpendicular to the flowstream, with $Re_\theta = 1200$.

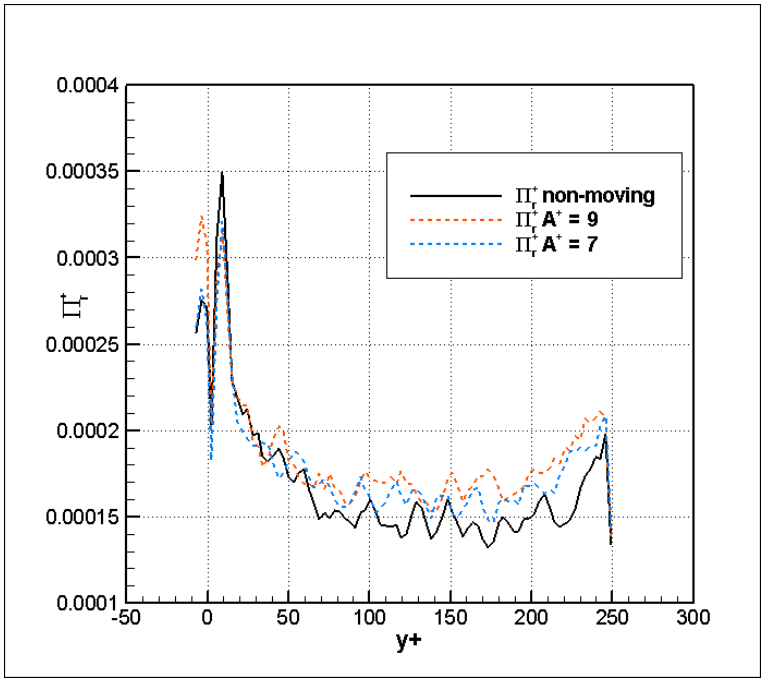

Figure 4.13: Streamwise positive $\left(\text{retrograde}, \Pi_r\right)$ vortex counting comparing three cases: non-actuated and two actuated cases, with varying amplitude. This counting refers to target areas perpendicular to the flowstream, with $Re_\theta = 1200$.

Chapter 5

Conclusions and Future Work

The impact of spanwise traveling transversal surface waves on the turbulent boundary layer flow has been investigated using PIV and μ-PTV measurements. The wave motion was generated by a newly developed electromagnetic actuator system connected to the lower side of an aluminum sheet which was part of a flat plate flow setup in a subsonic wind tunnel. The PIV and μ-PTV experiments have been conducted for three momentum thickness based Reynolds numbers $Re_\theta =$ 1200, 1660, and 2080. While the actuation wavelength and frequency have been kept constant, three amplitudes have been considered. The findings show a clear impact of the traveling wave on the velocity distribution in the viscous sublayer and the logarithmic region of the turbulent boundary layer downstream of the actuated surface. The transversal wave motion of the wall results in a redistribution of the turbulence content in the boundary layer. The velocity fluctuations in the outer boundary layer, i.e. $y^+ > 100$, increase and strongly interact with each other. This leads to a lower kinetic energy in the viscous sublayer which reduces the wall-shear stress distribution. The maximum drag reduction of 3.42% has been achieved for the lowest Reynolds number, i.e. $Re_\theta = 1200$, at the highest amplitude $A^+ = 9$. Increasing the Reynolds number to $Re_\theta = 2080$ resulted in either an insignificant drag reduction or even a slight drag increase. The comparison with results from Tamano and Itoh [34], who investigated the turbulent flow over a flexible sheet which underwent a traveling wave motion, shows a reasonable agreement for the low Reynolds number findings. Although the amplitudes of this study are lower than those of Tamano and Itoh, the results of this study evidence the reduction of the friction drag over an aluminum surface actuated by a spanwise transversal wave.

To further examine these findings, a thorough uncertainty analysis will have to be carried out in a future work. In this one, a methodology to ascertain the error associated with determining u_τ with a least square linear fitting in the viscous sublayer has been proposed. In addition, the systematic error associated with the manual positioning of grid points in the pre-processing software PIVmap® remains to be determined. Also, the impact of normalizing each velocity profile, either from an actuated or non-actuated case, with their intrinsic u_τ, rather than with the friction velocity of the non-actuated case, remains to be studied. The flow structure based on its vortex population densities has to be further discussed in order to attribute significance to the increase of streamwise

vortices detected inside the buffer layer.

The use of an aluminum surface makes it possible to combine passive and active drag reduction approaches. That is, in a future study, the aluminum surface could be provided of a riblet structure and this structured surface could undergo transversal wave motions. Considering this combination of active and passive flow control devices, relevant questions to be addressed are whether this combined passive-active setup will even lead to higher drag reduction or whether the high sensitivity of the drag reduction impact on the geometric measures of the riblet structure can be lowered such that an optimum drag reduction can be achieved at a broader Reynolds number range.

Appendix A

Matlab® routines

A.1 Reading PIVview® files

```
function [coordinates, data] = reading(path, filename)
global u v u_fluct v_fluct vort dudx dudy dvdx dvdy var_count sizeX sizeY;
    %Reads PIVview output .dat files and stores their content in data-cells
    root_dir = path;

    %Read averaged data
    fid_avg = fopen(strcat(root_dir,'\_avg','.dat'));
    results_avg = textscan(fid_avg,['%f %f %f %f %f %f %f %f %f %f %f %f'...
       '%f %f %f %f %f %f %f'],'headerlines',17 );
    fclose(fid_avg);
    temp_data=cell2mat(results_avg);

%     Get coordinates
    coordinates(:,1) = temp_data(:,1);
    coordinates(:,2) = temp_data(:,2);

%     Get dimensions of 2d array
    y_test = coordinates(1,2);
    k=0;
    file_length=size(coordinates,1);
    while y_test == coordinates(1,2)
        k=k+1;
        y_test = (coordinates(k,2));
    end
    sizeX = k-1;
    sizeY = file_length/sizeX;

%     Get average data
    data_average(:,u) = temp_data(:,3);
    data_average(:,v) = temp_data(:,4);
```

```
%     Get list of timeresolved results
    frm_name_files = sprintf('%s',root_dir,'\',filename,'*.dat')
    list_files = dir(frm_name_files);

    num_files = length(list_files)

%     Initialize data array
    data = zeros(size(coordinates,1),var_count,num_files);

%     Read files
    for n = 1:num_files
        disp(['Reading ',num2str(n),'/',num2str(num_files)]);
        fid = fopen(fullfile(root_dir, list_files(n).name));

        %number of headerlines for _avg.dat files = 17
        %number of headerlines for screenshot .dat files = 16
        %version 3.5.8.2: no. of headerlines for screenshot .dat files = 16
        inputdata = textscan(fid,['%f %f %f %f %f %f %f %f %f %f %f %f %f'...
            '%f %f %f %f %f %f'],'headerlines',16 );
        fclose(fid);
        temp_data = cell2mat(inputdata);

        data(:,u,n)=temp_data(:,3);
        data(:,v,n)=temp_data(:,4);
        data(:,u_fluct,n)=temp_data(:,3)-data_average(:,u);
        data(:,v_fluct,n)=temp_data(:,4)-data_average(:,v);
        data(:,vort,n)=temp_data(:,7);
        data(:,dudx,n)=temp_data(:,8);
        data(:,dudy,n)=temp_data(:,9);
        data(:,dvdx,n)=temp_data(:,10);
        data(:,dvdy,n)=temp_data(:,11);
    end
    clear temp_data;
end
```

A.2 Calculating swirling strength

```
function [ data ] = swirling_strength_calculation( data)
global u v u_fluct v_fluct u_mod v_mod vort dudx dudy dvdx dvdy triangle_ci ...
    triangle_ci_rms triangle_ci_rms_masked var_count sizeX sizeY;
    %For use with files obtained with PIVview version from Wenfeng's PC

    % Calculating the swirling strength (lamdba_ci) and modified
    % swirling strength parameter (triangle_ci) for a time-averaged velocity
    % vector field measured perpendicular to the flow stream.
    triangle_ci_squared_sum = zeros(size(data,1),1);
    triangle_ci_count = 0;
```

```
    disp('Calculating Swirling Strength...');
    for timestep=1:size(data,3)

        for datapoint=1:size(data,1)
            %creating temporary matrix containing local velocity gradient tensor
            A(1,1) = data(datapoint,dudx,timestep);
            A(1,2) = data(datapoint,dudy,timestep);
            A(2,1) = data(datapoint,dvdx,timestep);
            A(2,2) = data(datapoint,dvdy,timestep);
            %calculating eigen-values of A
            eig_vec = eig(A);

            %swirling strength is given by the absolute value of the imaginary
            %component of A's eigen-values
            lambda_ci = abs(imag(eig_vec(1)));
%             data2(datapoint,12,timestep) = lambda_ci;

            %introducing modified swirling strength parameter, triangle_ci,
            %getting its signal from vortic_z, preventing divide-by-zero error
            if data(datapoint,vort,timestep)~=0
                data(datapoint,triangle_ci,timestep) = lambda_ci* ...
                    data(datapoint,vort,timestep)/abs(data(datapoint,7,timestep));
            else
               data(datapoint,triangle_ci,timestep) = 0;
            end

        end

        % Build sum of squared triangle_ci for time-space rms calculation
        triangle_ci_squared_sum = triangle_ci_squared_sum + ...
            data(:,triangle_ci,timestep).^2;
        triangle_ci_count = triangle_ci_count + 1;

        disp(['Calculating Swirling Strength ', num2str(timestep),'/', ...
            num2str(size(data,3))]);
    end


    disp(['Calculating Swirling Strength time-space rms']);
%     Sum time-summed triangle_ci^2 over space (in x-direction)
    % Convert linear array to 2d array
    triangle_ci_squared_sum = vec2mat(triangle_ci_squared_sum, sizeX);
    % Sum along x-direction
    squared_sum = sum(triangle_ci_squared_sum,2);
    triangle_ci_count = triangle_ci_count * size(triangle_ci_squared_sum,2);

    %Build rms value from squared sum
    rms_value =  sqrt(squared_sum/triangle_ci_count)* ...
```

```
        ones(1,size(triangle_ci_squared_sum,2));

    %Reshape 2d array back to linear array
    rms_value = reshape(rms_value',[],1);

    for timestep=1:size(data,3)
        % Devide by rms_value
        data(:,triangle_ci_rms,timestep)=data(:,triangle_ci,timestep)./rms_value;

        % Set Inf and NaN values to zero
        data(~isfinite(data(:,triangle_ci_rms,timestep)),triangle_ci_rms,timestep)=0;
    end
end
```

A.3 Counting vortices

```
function [vortex_count_positive, vortex_count_negative, data] = ...
    vortex_count(data, threshold)
global u v u_fluct v_fluct u_mod v_mod vort dudx dudy dvdx dvdy ...
    triangle_ci triangle_ci_rms triangle_ci_rms_masked var_count sizeX sizeY;

disp('Counting vortices...');

thresholdMask = (abs(data(:,triangle_ci_rms,:)) > threshold);

% Initialize arrays
vortex_count_positive=zeros(sizeY,sizeX);
vortex_count_negative=zeros(sizeY,sizeX);

% data(:,14,:) = zeros(size(data,1),1,size(data,3)); %u_mod
% data(:,15,:) = zeros(size(data,1),1,size(data,3)); %v_mod
% data(:,18,:) = zeros(size(data,1),1,size(data,3)); %masked ...
        %triangle_ci/triangle_ci_rms

% Identify Vortices
for timestep=1:size(data,3)
    % Convert linear array to 2D array
    thresholdMask2D = vec2mat(thresholdMask(:,:,timestep), sizeX);

    %Calculate connected non-zero datapoints
    connections=bwconncomp(thresholdMask2D',4);

    % Run through all connected areas
    for vortex=1:connections.NumObjects
        %Get index list of connected datapoints for current vortex
        pixelList=connections.PixelIdxList{1,vortex};

        %Transform linear array indices to 2D indices
```

```
        [yPosition, xPosition]=ind2sub(sizeX,pixelList);

        %Size of bounding box of current vortex
        vortexWidth = max(xPosition)-min(xPosition)+1;
        vortexHeight = max(yPosition)-min(yPosition)+1;

        %Write areas larger then 3x3 to validConnections
        if (vortexWidth >=3 && vortexHeight >=3)
            %Vortex Diameter
            vortex_diameter = (vortexWidth+vortexHeight)/2;

            %Calculate modified velocity based on local galilean
            % decomposition: u' and v' for current vortex
            u_localMean=mean(data(pixelList,u,timestep));
            v_localMean=mean(data(pixelList,v,timestep));
            data(pixelList,u_mod,timestep) = data(pixelList,u,timestep)- ...
                u_localMean;
            data(pixelList,v_mod,timestep) = data(pixelList,v,timestep)- ...
                v_localMean;

            %Write masked triangle_ci/triangle_ci_rms
            data(pixelList,triangle_ci_rms_masked,timestep) = data(pixelList,...
                triangle_ci_rms,timestep);

            % Get maximum of absolute value of current vortex and index of
            % maximum
            [maxSwirl, maxIndexInPixelList] = max(abs(data(pixelList, ...
                triangle_ci_rms, timestep)));

            maxIndex = pixelList(maxIndexInPixelList);

            % Transform linear index of maximum to 2D index
            [xMaxPosition,yMaxPosition]=ind2sub(sizeX, maxIndex);

            % Add 1 to vortex_count array at position of maximum
            if (data(maxIndex, triangle_ci_rms, timestep)>0)
                vortex_count_positive(yMaxPosition, xMaxPosition) = ...
                    vortex_count_positive(yMaxPosition, xMaxPosition) + 1;
            elseif (data(maxIndex, triangle_ci_rms, timestep)<0)
                vortex_count_negative(yMaxPosition, xMaxPosition) = ...
                    vortex_count_negative(yMaxPosition, xMaxPosition) + 1;
            else
                error(['Something strange has happened. Swirling strength' ...
                'should be non-zero']);
            end
        end
    end
%     imagesc(vortex_count_positive)
%     imagesc(vec2mat(data(:,17,1),84))
```

```
    disp(['Counting vortices ', num2str(timestep),'/',num2str(size(data,3))]);
end

end
```

A.4 Printing results from swirling strength calculation

```
function [] = save2text_swirl_strength(output_index, coordinates, data, u_tau, ...
    case_description, output_path)
global u v u_fluct v_fluct u_mod v_mod vort dudx dudy dvdx dvdy triangle_ci ...
    triangle_ci_rms triangle_ci_rms_masked var_count sizeX sizeY;
%   Prints out the swirling strength lambda_ci and modified swirling
%   strength parameter results from a arbitrary screenshot to a .dat file

    nu = 15.36*10^(-6); %m^2/s (kinematic viscosity of air)

    disp('Writing snapshots');

    % Write tecplot Header
    fid=fopen([output_path, '\swirl_strength', case_description,'.dat'],'wt');
    fprintf(fid, strcat('TITLE = "PIV Data | Parallel to Flow |',...
        case_description,'"\n'));
    fprintf(fid, ['VARIABLES = "x", "y", "x+", "y+", "u", "v", "u+", "v+", ' ...
        '"Vorticity", "triangle", "triangle_normalized",' ...
        '"triangle_normalized(masked)", "umod", "vmod", "umod+", "vmod+"\n']);

    %results is the matrix that will store the data for printing
    results = zeros(size(data,1),16);

    for zone=output_index
    %     Write Zone Header
        fprintf(fid, 'Zone T="%s, timestep %i", I=%i, J=%i\n',...
            case_description, zone, sizeX, sizeY);

        results(:,1) = coordinates(:,1); %x
        results(:,2) = coordinates(:,2); %y
        results(:,3) = coordinates(:,1)*u_tau/nu*0.001; %x+
        results(:,4) = coordinates(:,2)*u_tau/nu*0.001; %y+
        results(:,5) = data(:,u,zone); %u
        results(:,6) = data(:,v,zone); %v
        results(:,7) = data(:,u,zone)/u_tau; %u+
        results(:,8) = data(:,v,zone)/u_tau; %v+
        results(:,9) = data(:,vort,zone); %vorticity
        results(:,10) = data(:,triangle_ci,zone); %triangle_ci
        results(:,11) = data(:,triangle_ci_rms,zone); %triangle_ci/triangle_ci_rms
        results(:,12) = data(:,triangle_ci_rms_masked,zone); ...
            %masked triangle_ci/triangle_ci_rms
        results(:,13) = data(:,u_mod,zone); %u_mod
```

```
        results(:,14) = data(:,v_mod,zone); %v_mod
        results(:,15) = data(:,u_mod,zone)/u_tau; %u_mod+
        results(:,16) = data(:,v_mod,zone)/u_tau; %v_mod+

        fprintf(fid, '%e %e %e %e %e %e %e %e %e %e %e %e %e %e %e %e\n', results');
        disp(['...timestep ',num2str(zone),' written.']);
    end

    fclose(fid);

end
```

A.5 Printing results from vortex counting

```
function [] = save2text_vortex_count(coordinates, data, count_positive,...
    count_negative, u_tau, delta, case_description, output_path)
global u v u_fluct v_fluct u_mod v_mod vort dudx dudy dvdx dvdy ...
    triangle_ci triangle_ci_rms triangle_ci_rms_masked var_count sizeX sizeY;

    nu = 15.36*10^(-6); %m^2/s (kinematic viscosity of air)

    disp('Writing vortex count');

    % Sum count in x-direction
    count_positive_y_profile = sum(count_positive,2);
    count_negative_y_profile = sum(count_negative,2);

    %%%%%% Streamwise field of view
    %Transform x-coordinate to 2d array
    x_coordinates = vec2mat(coordinates(:,1), sizeX);
    %Average position along y-direction
    x_position = mean(x_coordinates,1);
    Lx = x_position(end) - x_position(1); %field of view in mm

    %%%%%% Get y-position from coordinates array
    %Transform y-coordinate to 2d array
    y_coordinates = vec2mat(coordinates(:,2), sizeX);
    %Average position along x-direction
    y_position = mean(y_coordinates,2);

    density_positive = zeros(1,length(y_position));
    density_negative = zeros(1,length(y_position));
    density_positive_nondim = zeros(1,length(y_position));
    density_negative_nondim = zeros(1,length(y_position));

    for y=2:length(count_positive_y_profile)-1
        % Calculate delta y as central difference
        delta_y = (y_position(y+1)-y_position(y-1))/2;
```

```
    % Count of vortices in 3 delta_y * L area, with L:
    % streamwise field of view
    positive = (count_positive_y_profile(y-1)+ ...
        count_positive_y_profile(y)+count_positive_y_profile(y+1));
    negative = (count_negative_y_profile(y-1)+ ...
        count_negative_y_profile(y)+count_negative_y_profile(y+1));

    %Divide count of vortices by number of timesteps to get ensemble...
    %averaged count
    positive = positive / size(data, 3);
    negative = negative / size(data, 3);

    % Calculate density
    density_positive(y) = positive/(3*delta_y/delta*Lx/delta);
    density_negative(y) = negative/(3*delta_y/delta*Lx/delta);

    % Calculate nondimensional
    density_positive_nondim(y) = positive/(3*delta_y*u_tau/nu*0.001* ...
        Lx*u_tau/nu*0.001);
    density_negative_nondim(y) = negative/(3*delta_y*u_tau/nu*0.001* ...
        Lx*u_tau/nu*0.001);
end

% Write Tecplot header
fid=fopen([output_path, '\vortex_count', case_description,'.dat'],'wt');
fprintf(fid, strcat('TITLE = "',case_description,'"\n'));
fprintf(fid, ['VARIABLES = "y", "y+", "<greek>P</greek><sub>r</sub>",'...
    '"<greek>P</greek><sub>p</sub>", "<greek>P</greek><sup>+</sup><sub>r</sub>",'...
    '"<greek>P</greek><sup>+</sup><sub>p</sub>"\n']);

%results is the matrix that will store the data for printing
results = zeros(length(y_position)-2,6);

%     Write Zone Header
fprintf(fid, 'Zone T="%s", I=%i, J=1\n',case_description, size(results,1));

results(:,1) = y_position(2:end-1); %y
results(:,2) = y_position(2:end-1) * u_tau/nu*0.001; %y+
results(:,3) = density_positive(2:end-1); %Density positive/retrograde
results(:,4) = density_negative(2:end-1); %Density negative/prograde
results(:,5) = density_positive_nondim(2:end-1); %Non-dimensional ...
    % density positive/retrograde
results(:,6) = density_negative_nondim(2:end-1); %Non-dimensional
    % density negative/prograde

fprintf(fid, '%e %e %e %e %e %e\n', results');

fclose(fid);
```

```
    % Write Tecplot header
    fid=fopen([output_path, '\vortex_count_spatial', case_description,'.dat'],'wt');
    fprintf(fid, strcat('TITLE = "',case_description,'"\n'));
    fprintf(fid, ['VARIABLES = "x", "y", "x+", "y+", "N<sub>r</sub>",'...
        '"N<sub>p</sub>"\n']);

    %results is the matrix that will store the data for printing
    results = zeros(size(coordinates,1),6);

    %     Write Zone Header
    fprintf(fid, 'Zone T="%s", I=%i, J=%i\n',case_description, sizeX, sizeY);

    results(:,1) = coordinates(:,1); %x
    results(:,2) = coordinates(:,2); %y
    results(:,3) = coordinates(:,1) * u_tau/nu*0.001; %x+
    results(:,4) = coordinates(:,2) * u_tau/nu*0.001; %y+
%     results(:,5) = reshape(count_positive',[],1);
          %Total count positive/retrograde
%     results(:,6) = reshape(count_negative',[],1);
          %Total count negative/prograde
    results(:,5) = reshape(count_positive',[],1)/size(data,3); %Time Average ...
              %count positive/retrograde
    results(:,6) = reshape(count_negative',[],1)/size(data,3); %Time Average ...
              %count negative/prograde

    fprintf(fid, '%e %e %e %e %e %e\n', results');

    fclose(fid);
end
```

A.6 Running script

```
clc;
% clear;
input_directory='\a=0.375\24x24';
output_directory='\results in graphics\a=0.375';
input_filename='8ms';
input_description='_perp_24x24_a=0.375';
output_timesteps = 50;
root_path='C:\Users\Rui\Dropbox\AIA\RESULTS\resutls PIV perpendicular to the flow';
threshold = 1.5;
u_tau =0.372; %m/s (friction velocity for u_free_stream = 8 m/s)
delta = 25; %boundary layer thickness

% Define indices of data array
global u v u_fluct v_fluct u_mod v_mod vort dudx dudy dvdx dvdy triangle_ci triangle_ci_rms
u=1; v=2; u_fluct=3; v_fluct=4; u_mod=5; v_mod=6; vort=7; dudx=8; dudy=9; dvdx=10; dvdy=11;
```

```
% Read data
[coordinates, data] = reading([root_path, input_directory], input_filename);

% Calculate Swirling strength, swirling strength parameter and normalized
% swirling strength parameter
data=swirling_strength_calculation(data);

% imagesc(vec2mat(data(:,triangle_ci_rms,1),sizeX));

% Count vortices and calculate modified velocity
[count_positive, count_negative, data] = vortex_count(data, threshold);

% imagesc(vec2mat(data(:,triangle_ci_rms_masked,1),sizeX));

% Save instantaneous swirling strength field
save2text_swirl_strength(output_timesteps, coordinates, data, u_tau, input_description, [root_path

save2text_vortex_count(coordinates, data, count_positive, count_negative, u_tau, delta, input_desc

% for n=1:19
%     input(:,:,n)=vec2mat(data(:,n,1),84);
%     swirl(:,:,n)=vec2mat(data2(:,n,1),84);
%     fluct(:,:,n)=vec2mat(data_fluct(:,n,1),84);
%     rms(:,:,n)=vec2mat(data_rms(:,n),84);
%     avg(:,:,n)=vec2mat(data_avg(:,n),84);
% end

disp('Done.');
```

Appendix B

Preliminary analysis of experimental uncertainty

B.1 Uncertainty of the friction velocity

In this work, the friction velocity u_τ has been indirectly determined through a least square linear fitting in the viscous sublayer. Ascertaining its experimental uncertainty and how the error propagates to the final derived results is of paramount importance.

As such, we propose the following reasoning, starting with a brief mention to the general case of calculating an uncertainty from a result expressed in a data-reduction equation.

So, assuming that the experimental result, r, is a function of J variables X_i, expressed in a data-reduction equation of this kind:

$$r = r(X_1, X_2, \ldots, X_J) \tag{B.1}$$

then its uncertainty is given by [35]:

$$U_r^2 = \left[\left(\frac{\partial r}{\partial X_1} U_{X_1} \right)^2 + \left(\frac{\partial r}{\partial X_2} U_{X_2} \right)^2 + , \ldots , + \left(\frac{\partial r}{\partial X_J} U_{X_J} \right)^2 \right] \tag{B.2}$$

Equation (B.2) can be non-dimensionalized by dividing it by r, yielding [35]:

$$\frac{U_r^2}{r^2} = \left(\frac{X_1}{r} \frac{\partial r}{\partial X_1} \right)^2 \left(\frac{U_{X_1}}{X_1} \right)^2 + \left(\frac{X_2}{r} \frac{\partial r}{\partial X_2} \right)^2 \left(\frac{U_{X_2}}{X_2} \right)^2 + , \ldots , + \left(\frac{X_J}{r} \frac{\partial r}{\partial X_J} \right)^2 \left(\frac{U_{X_J}}{X_J} \right)^2 \tag{B.3}$$

In the particular case when the data-reduction equation is of the form $r = kX_1^a X_2^b X_3^c \cdots$, Equation (B.3) simplifies to [35]:

$$\frac{U_r^2}{r^2} = a^2 \left(\frac{U_{X_1}}{X_1} \right)^2 + b^2 \left(\frac{U_{X_2}}{X_2} \right)^2 + c^2 \left(\frac{U_{X_3}}{X_3} \right)^2 + \cdots \tag{B.4}$$

We now proceed to apply the aforementioned to our case. The linear relationship $u^+ = y^+$ is valid for $y^+ < 5$. From visual inspection of u *vs* y data, this relationship appears to be valid at least in the nearest $N = 10$ data points from the wall. As such, a linear fitting $\mathbf{Y} = m\mathbf{X}$ is applied, where the vectors $\mathbf{X}$ and $\mathbf{Y}$ take accordingly the values of y and u pertaining to those 10 points. From the boundary layer theory, the linear relationship is known to be of the form:

$$u = \frac{u_\tau^2}{\nu} y \tag{B.5}$$

and therefore the slope m corresponds to

$$m = \frac{du}{dy} = \frac{u_\tau^2}{\nu} \tag{B.6}$$

Knowing the kinematic viscosity ν the results from this regression allow for the determination of u_τ. Furthermore, the uncertainty of m ($m \pm U_m$) is also calculable through the regression, making use of the following equations [35]:

$$U_m = t \cdot S_m \tag{B.7a}$$

$$S_m = \sqrt{\frac{S_Y^2}{S_{XX}}} \tag{B.7b}$$

$$S_{XX} = \sum_{i=1}^{N} X_i^2 - \frac{1}{N}\left(\sum_{i=1}^{N} X_i\right)^2 \tag{B.7c}$$

$$S_Y = \sqrt{\frac{1}{N-2}\sum_{i=1}^{N}(Y_i - Y_{\text{fit},i})^2} \tag{B.7d}$$

Here, X_i and Y_i represent respectively the individual values of y and u in each point of measurement. The quantity denoted by $Y_{\text{fit},i}$ is the value of velocity calculated through the fit.

Setting a confidence level of 95%, the value of t retrieved from a Student's t-distribution, in which the degrees of freedom are $\nu = N - 2 = 8$, is $t = 2.31$.

B.2 Propagation of the error into the derived results

Knowing U_m, calculated in the previous section, the uncertainty in the drag reduction can be determined by exploring the propagation of error affecting each of the derived results in this chain: $U_m \rightarrow u_\tau \rightarrow \tau_w \rightarrow c_f \rightarrow$ DR. Applying Equation (B.4) to the first element of this chain yields:

$$\frac{U_m}{m} = \sqrt{\left(2\frac{U_{u_\tau}}{u_\tau}\right)^2 + \cancel{\left(\frac{U_\nu}{\nu}\right)}} \approx 0 \tag{B.8a}$$

$$\Leftrightarrow \frac{U_{u_\tau}}{u_\tau} = \frac{1}{2}\frac{U_m}{m} \tag{B.8b}$$

On the other hand, one can also observe that

$$\tau_w \approx \mu \left.\frac{du}{dy}\right|_{y=0} = \mu \cdot m \tag{B.9a}$$

$$\tau_w \approx \mu \left.\frac{du}{dy}\right|_{y=0} = \mu \cdot \frac{u_\tau^2}{\nu} \tag{B.9b}$$

Resorting once again to Equation (B.4), the uncertainty of τ_w can be derived:

$$\frac{U_{\tau_w}}{\tau_w} = \sqrt{\left(\frac{U_m}{m}\right)^2 + \cancelto{\approx 0}{\left(\frac{U_\nu}{\nu}\right)^2}} \tag{B.10a}$$

$$\Leftrightarrow \frac{U_{\tau_w}}{\tau_w} = \frac{U_m}{m} \tag{B.10b}$$

This uncertainty of τ_w can also be expressed in terms of the uncertainty of u_τ, acknowledging that $U_m/m = 2\,U_{u_\tau}/u_\tau$ (via Equation (B.8b)):

$$\frac{U_{\tau_w}}{\tau_w} = 2\,\frac{U_{u_\tau}}{u_\tau} \tag{B.10c}$$

Since c_f is given by

$$c_f = \frac{\tau_w}{1/2 \cdot \rho \cdot u_\infty^2} \tag{B.11}$$

its uncertainty can also be computed with Equation (B.4):

$$\frac{U_{c_f}}{c_f} = \sqrt{\left(\frac{U_{\tau_w}}{\tau_w}\right)^2 + 4\left(\frac{U_{u_\infty}}{u_\infty}\right)^2} \tag{B.12a}$$

$$\Leftrightarrow \frac{U_{c_f}}{c_f} = \sqrt{4\left(\left(\frac{U_{u_\tau}}{u_\tau}\right)^2 + \left(\frac{U_{u_\infty}}{u_\infty}\right)^2\right)} \tag{B.12b}$$

By definition, the drag reduction registered in a general case 1 compared to a reference case 0 is given by:

$$\mathrm{DR} = 1 - \frac{c_{f,1}}{c_{f,0}} \tag{B.13}$$

Since this quantity is not of the form $r = kX_1^a X_2^b X_3^c \cdots$, the more general formula of uncertainty (Equation (B.2)), must be used:

$$U_{\mathrm{DR}} = \left[\left(\frac{\partial \mathrm{DR}}{\partial c_{\mathrm{f},1}} U_{c_{\mathrm{f},1}} \right)^2 + \left(\frac{\partial \mathrm{DR}}{\partial c_{\mathrm{f},0}} U_{c_{\mathrm{f},0}} \right)^2 \right]^{\frac{1}{2}} \tag{B.14a}$$

$$\Leftrightarrow U_{\mathrm{DR}} = \left[\left(-\frac{1}{c_{\mathrm{f},2}} U_{c_{\mathrm{f},1}} \right)^2 + \left(\frac{c_{\mathrm{f},1}}{c_{\mathrm{f},0}^2} U_{c_{\mathrm{f},0}} \right)^2 \right]^{\frac{1}{2}} \tag{B.14b}$$

$$\Leftrightarrow U_{\mathrm{DR}} = \left[\frac{1}{c_{\mathrm{f},0}^2} \cdot 4 \left[\left(\frac{U_{u_{\tau,1}}}{u_{\tau,1}} \right)^2 + \left(\frac{U_{u_{\infty,1}}}{u_{\infty,1}} \right)^2 \right] \cdot c_{\mathrm{f},1}^2 + \right.$$

$$\left. + \frac{c_{\mathrm{f},1}^2}{c_{\mathrm{f},0}^4} \cdot 4 \left[\left(\frac{U_{u_{\tau,0}}}{u_{\tau,0}} \right)^2 + \left(\frac{U_{u_{\infty,0}}}{u_{\infty,0}} \right)^2 \right] \cdot c_{\mathrm{f},0}^2 \right]^{\frac{1}{2}} \tag{B.14c}$$

$$\Leftrightarrow U_{\mathrm{DR}} = \sqrt{4 \left(\frac{c_{\mathrm{f},1}}{c_{\mathrm{f},0}} \right)^2 \left[\left(\frac{U_{u_{\tau,1}}}{u_{\tau,1}} \right)^2 + \left(\frac{U_{u_{\infty,1}}}{u_{\infty,1}} \right)^2 + \left(\frac{U_{u_{\tau,0}}}{u_{\tau,0}} \right)^2 + \left(\frac{U_{u_{\infty,0}}}{u_{\infty,0}} \right)^2 \right]} \tag{B.14d}$$

Equation (B.14d) can then be used to compute the uncertainty of DR.

$$\omega_z = \frac{\partial v}{\partial x} - \frac{\partial u}{\partial y} \tag{B.15}$$

References

[1] Géza Schrauf. Katnet - key aerodynamic technologies for aircraft performance improvement. 5th Community Aeronautical Days, 2006.

[2] Luciano Castillo, Xia Wang, and William K George. Separation criterion for turbulent boundary layers via similarity analysis. *Journal of fluids engineering*, 126(3):297–304, 2004.

[3] S. J. Kline, W. C. Reynolds, F. A. Schraub, and P. W. Runstadler. The structure of turbulent boundary layers. *Journal of Fluid Mechanics*, 30:741–773, 12 1967.

[4] J. Lin, J.P. Laval, J.M. Foucaut, and M. Stanislas. Quantitative characterization of coherent structures in the buffer layer of near-wall turbulence. part 1: streaks. *Experiments in Fluids*, 45(6):999–1013, 2008.

[5] G. E. Karniadakis and Kwing-So Choi. Mechanisms on transverse motions in turbulent wall flows. *Annu. Rev. Fluid Mechanics*, 35:45–62, 2003.

[6] Jung, W.J. and Mangiavacchi, N. and Akhavan, R. Suppression of turbulence in wall-bounded flows by high-frequency spanwise oscillations. *Physics of Fluids*, 4, 1992.

[7] Thomas R. Bewley. Flow control: new challenges for a new renaissance. *Progress in Aerospace Sciences*, 37(1):21 – 58, 2001.

[8] Touber, P., Leschziner, M. Near-wall streak modification by spanwise oscillatory wall motion and drag-reduction mechanisms. *Journal of Fluid Mechanics*, pages 1–51, 2012.

[9] L. Agostini, E. Touber, and M. A. Leschziner. Spanwise oscillatory wall motion in channel flow: drag-reduction mechanisms inferred from dns-predicted phase-wise property variations at re-tau=1000. *Journal of Fluid Mechanics*, 743:606–635, MAR 2014.

[10] Y. Du, V. Symeonidis, and G. E. Karniadakis. Drag reduction in wall-bounded turbulence via a transverse travelling wave. *Journal of Fluid Mechanics*, 457:1–34, April 2002.

[11] Timothy W. Berger, John Kim, Changhoon Lee, and Junwoo Lim. Turbulent boundary layer control utilizing the lorentz force. *Physics of Fluids (1994-present)*, 12(3):631–649, 2000.

[12] Kenneth S. Breuer, Jinil Park, and Charles Henoch. Actuation and control of a turbulent channel flow using lorentz forces. *Physics of Fluids (1994-present)*, 16(4):897–907, 2004.

[13] Du, Yiqing and Karniadakis, George Em. Suppressing wall turbulence by means of a transverse traveling wave. *Science*, 288, 2000.

[14] Maurizio Quadrio, Pierre Ricco, and Claudio Viotti. Streamwise-travelling waves of spanwise wall velocity for turbulent drag reduction. *Journal of Fluid Mechanics*, 627:161–178, 5 2009.

[15] P. Ricco. Modification of near-wall turbulence due to spanwise wall oscillations. *Journal Of Turbulence*, 5(1):1 – 18, 2004.

[16] Zhou, D. and Ball, K . S. The mechanism of turbulent drag reduction by spanwise wall oscillation. *Joint Propulsion Conferece & Exhibit*, pages 1 – 14, 2006.

[17] R. Akhavan, W. J. Jung, and N. Mangiavacchi. Turbulence control in wall-bounded flows by spanwise oscillations. *Applied Scientific Research*, 51(1-2):299–303, 1993.

[18] Baron, Arturo and Quadrio, Maurizio. Turbulent drag reduction by spanwise wall oscillations. *Applied Scientific Research*, 55:311–326, 1996.

[19] Kwing-So Choi. Near-wall structure of turbulent boundary layer with spanwise-wall oscillation. *Physics of Fluids (1994-present)*, 14(7):2530–2542, 2002.

[20] Dantec Dynamics - Laser Optical Measurements Systems and Sensors. Particle image velocimetry - educational poster, August 2014.

[21] Markus Raffel, Christian E. Willert, Steve T. Wereley, and Jürgen Kompenhans. *Particle Image Velocimetry*. Springer-Verlag Berlin Heidelberg, 2nd edition, 2007.

[22] Jerry Westerweel and Fulvio Scarano. Universal outlier detection for piv data. *Experiments in Fluids*, 39(6):1096–1100, 2005.

[23] John C. Crocker and David G. Grier. Methods of digital video microscopy for colloidal studies. *Journal of Colloid and Interface Science*, 179(1):298 – 310, 1996.

[24] H.G. Maas, A. Gruen, and D. Papantoniou. Particle tracking velocimetry in three-dimensional flows. *Experiments in Fluids*, 15(2):133–146, 1993.

[25] J Westerweel. Fundamentals of digital particle image velocimetry. *Measurement Science and Technology*, 8(12):1379, 1997.

[26] Bertrand Lecordier and Michel Trinité. Accuracy assessment of image interpolation schemes for piv from real images of particle. In *Proc. 13th int. symp. on appl. of laser techn. to fluid mechanics, Lisbon, Portugal*, 2006.

[27] L. H. Benedict and R. D. Gould. Towards better uncertainty estimates for turbulence statistics. *Experiments in Fluids*, 22(2):129–136, 1996.

[28] R. J. Adrian, K. T. Christensen, and Z.-C. Liu. Analysis and interpretation of instantaneous turbulent velocity fields. *Experiments in Fluids*, 29(3):275–290, 2000.

[29] M. S. Chong, A. E. Perry, and B. J. Cantwell. A general classification of three-dimensional flow fields. *Physics of Fluids A: Fluid Dynamics (1989-1993)*, 2(5):765–777, 1990.

[30] Jigen Zhou, Ronald J. Adrian, and S. Balachandar. Autogeneration of near-wall vortical structures in channel flow. *Physics of Fluids (1994-present)*, 8(1):288–290, 1996.

[31] J. Zhou, R. J. Adrian, S. Balachandar, and T. M. Kendall. Mechanisms for generating coherent packets of hairpin vortices in channel flow. *Journal of Fluid Mechanics*, 387:353–396, 5 1999.

[32] Sang-Joon Lee and Yong-Seok Choi. Decrement of spanwise vortices by a drag-reducing riblet surface. *Journal of Turbulence*, page N23, 2008.

[33] Y. Wu and K. T. Christensen. Population trends of spanwise vortices in wall turbulence. *Journal of Fluid Mechanics*, 568:55–76, 12 2006.

[34] Shinji Tamano and Motoyuki Itoh. Drag reduction in turbulent boundary layers by spanwise traveling waves with wall deformation. *Journal of Turbulence*, page N9, 2012.

[35] Paulo Coelho. *Experiments and Uncertainty Analysis (Experimentação e Análise de Incertezas) - teaching notes*. Department of Mechanical Engineering - Faculty of Engineering - University of Porto, September 2013.